

## THE TWO YOUNG STAR DISKS IN THE CENTRAL PARSEC OF THE GALAXY: PROPERTIES, DYNAMICS, AND FORMATION<sup>1</sup>

T. PAUMARD,<sup>2</sup> R. GENZEL,<sup>2,3</sup> F. MARTINS,<sup>2</sup> S. NAYAKSHIN,<sup>4,5</sup> A. M. BELOBORODOV,<sup>6,7</sup> Y. LEVIN,<sup>8,9</sup> S. TRIPPE,<sup>2</sup> F. EISENHAUER,<sup>2</sup>  
T. OTT,<sup>2</sup> S. GILLESSEN,<sup>2</sup> R. ABUTER,<sup>2</sup> J. CUADRA,<sup>4</sup> T. ALEXANDER,<sup>10,11</sup> AND A. STERNBERG<sup>12</sup>

Received 2005 November 8; accepted 2006 January 31

### ABSTRACT

We report the definite spectroscopic identification of  $\simeq 40$  OB supergiants, giants, and main-sequence stars in the central parsec of the Galaxy. Detection of their absorption lines has become possible with the high spatial and spectral resolution and sensitivity of the adaptive optics integral field spectrometer SPIFFI/SINFONI on the ESO VLT. Several of these OB stars appear to be helium- and nitrogen-rich. Almost all of the  $\simeq 80$  massive stars now known in the central parsec (central arcsecond excluded) reside in one of two somewhat thick ( $\langle |h|/R \rangle \simeq 0.14$ ) rotating disks. These stellar disks have fairly sharp inner edges ( $R \simeq 1''$ ) and surface density profiles that scale as  $R^{-2}$ . We do not detect any OB stars outside the central 0.5 pc. The majority of the stars in the clockwise system appear to be on almost circular orbits, whereas most of those in the “counterclockwise” disk appear to be on eccentric orbits. Based on its stellar surface density distribution and dynamics, we propose that IRS 13E is an extremely dense cluster ( $\rho_{\text{core}} \gtrsim 3 \times 10^8 M_{\odot} \text{pc}^{-3}$ ) that has formed in the counterclockwise disk. The stellar contents of both systems are remarkably similar, indicating a common age of  $\simeq 6 \pm 2$  Myr. The  $K$ -band luminosity function of the massive stars suggests a top-heavy mass function and limits the total stellar mass contained in both disks to  $\simeq 1.5 \times 10^4 M_{\odot}$ . Our data strongly favor in situ star formation from dense gas accretion disks for the two stellar disks. This conclusion is very clear for the clockwise disk and highly plausible for the counterclockwise system.

*Subject headings:* Galaxy: center — stars: early-type — stars: formation —  
stars: luminosity function, mass function — stellar dynamics

*Online material:* color figures, machine-readable table

### 1. INTRODUCTION

The Galactic center (GC) is a unique laboratory for studying galactic nuclei. Given its proximity, processes in the GC can be investigated at resolutions and detail that are not accessible in any other galactic nucleus (unless otherwise specified, we adopt a distance of 8 kpc for simplicity of comparison to earlier work; we specifically use the most recent value  $R_0 = 7.62 \pm 0.32$  kpc by Eisenhauer et al. [2005] when the  $\simeq 5\%$  error could lead to a significant bias). The GC has many features that are thought to occur in other nuclei (for reviews see Genzel & Townes 1987; Morris &

Serabyn 1996; Mezger et al. 1996; Alexander 2005). It contains the densest star cluster in the Milky Way intermixed with a bright H II region (Sgr A West or the “minispiral”) and hot gas radiating at X-rays. These central components are surrounded by a  $\simeq 1.5$  pc ring/torus of dense molecular gas (the “circumnuclear disk” [CND]). At the very center lies a very compact radio source, Sgr A\*. The short orbital period of stars (in particular the B star S2) in the central arcsecond around Sgr A\* shows that the radio source is a  $(3-4) \times 10^6 M_{\odot}$  black hole (BH) beyond any reasonable doubt (Schödel et al. 2002; Ghez et al. 2003). The larger GC region contains three remarkably rich clusters of young, high-mass stars: the Quintuplet, the Arches, and the parsec-scale cluster around Sgr A\* itself (Figer 2003).

In seeing-limited near-infrared images of the central region of the GC, several bright sources dominate the  $\simeq 20'' \times 20''$  field centered on Sgr A\*. Among these, the IRS 16 cluster<sup>13</sup> (Becklin & Neugebauer 1975) is a bright source of broad He I 2.058  $\mu\text{m}$  line emission (Hall et al. 1982). IRS 16 has been since then resolved into a cluster of about a half-dozen stars (Forrest et al. 1987; Allen et al. 1990; Krabbe et al. 1991, 1995; Tamblyn et al. 1996; Paumard et al. 2001). These appear to be post-main-sequence OB stars in a transitional phase of high mass loss (Morris et al. 1996), between extreme O supergiants and Wolf-Rayet (W-R) stars (Allen et al. 1990; Najarro et al. 1994, 1997; Trippe et al. 2006). They have been classified as Ofpe/WN9 stars (Allen et al. 1990) and have been suggested as nitrogen-rich OB stars (OBN) by Hanson et al. (1996) and as luminous blue variable (LBV) candidates by Paumard et al. (2001). There is no a priori incompatibility between these tentative classifications that are

<sup>1</sup> Based on observations with the Very Large Telescope of the European Southern Observatory, Paranal, Chile.

<sup>2</sup> Max-Planck-Institut für extraterrestrische Physik (MPE), Giessenbachstrasse Postfach 1312, 85748 Garching, Germany; paumard@mpe.mpg.de, genzel@mpe.mpg.de.

<sup>3</sup> Department of Physics, University of California, 366 LeConte Hall, Berkeley, CA 94720.

<sup>4</sup> Max-Planck-Institut für Astrophysik (MPA), Karl-Schwarzschild-Strasse 1, 85741 Garching, Germany.

<sup>5</sup> Theoretical Astrophysics Group, Department of Physics and Astronomy, University of Leicester, University Road, Leicester LE1 7RH, UK.

<sup>6</sup> Physics Department and Columbia Astrophysics Laboratory, Columbia University, 1027 Pupin Hall, Mail Code 5247, New York, NY 10027.

<sup>7</sup> Astro Space Center, Russian Academy of Sciences, Lebedev Physical Institute, Profsoyuznaya 84/32, 117997 Moscow, Russia.

<sup>8</sup> Canadian Institute for Theoretical Astrophysics, University of Toronto, 60 St. George Street, Toronto, ON M5S 3H8, Canada.

<sup>9</sup> Sterrewacht Leiden, Leiden University, P.O. Box 9513, NL-2300 RA Leiden, Netherlands.

<sup>10</sup> Faculty of Physics, Weizmann Institute of Science, P.O. Box 26, Rehovot 76100, Israel.

<sup>11</sup> William Z. and Eda Bess Novick career development chair.

<sup>12</sup> School of Physics and Astronomy, Tel Aviv University, P.O. Box 39040, Tel Aviv 69978, Israel.

<sup>13</sup> The sources named “GCIRS” for Galactic Center Infrared Source are often referred to simply as “IRS” sources in the GC-centric literature.

based on different properties. Several dozens of even more evolved W-R stars have been observed in the same region (e.g., Krabbe et al. 1995; Blum et al. 1995; Paumard et al. 2001). The lack of OB stars in these earlier studies is puzzling. The question is whether this lack is due to a true depletion or is merely a selection effect due to veiling of the weak absorption lines in near-main-sequence stars by bright nebular emission. Adaptive optics (AO) spectroscopy of the centermost arcsecond around Sgr A\* (mostly devoid of nebular emission) has already revealed a dozen massive stars. These stars appear to be main-sequence late O and B stars and orbit the central BH at distances as short as a few light-days (Schödel et al. 2003; Ghez et al. 2003, 2005; Eisenhauer et al. 2005).

These observations show that massive star formation has occurred at or near the GC within the last few million years. This is surprising. All obvious routes to creating or bringing massive young stars in(to) the central region face major obstacles. In situ star formation, transport of stars from far out, scattering of stars on highly elliptical orbits, and rejuvenation of old stars due to stellar collisions and tidal stripping have all been proposed and considered (for a recent review of the rapidly growing body of literature see Alexander 2005). No explanation at this point is the obvious winner (or loser). Perhaps the two most prominent and promising scenarios for explaining the young massive stars outside the central cusp, at radii of  $3''$ – $10''$  from Sgr A\*, are the following:

1. The “in situ, accretion disk” scenario (Levin & Beloborodov 2003; Genzel et al. 2003; Goodman 2003; Milosavljevic & Loeb 2004; Nayakshin & Cuadra 2005). Here the proposal is that stars have formed near where they are found today, very close to the central BH. However, in situ star formation is impeded by the tidal shear from the central BH and surrounding dense star cluster. To overcome this shear, gas clouds have to be much denser ( $\approx 10^{12} R_{1''}^{-3} \text{ cm}^{-3}$ ) than currently observed (Morris 1993). The tidal shear can be overcome if the mass accretion was large enough at some point in the past—perhaps as the consequence of the infall and cooling of a large interstellar cloud—such that a gravitationally unstable (outside of a critical radius) disk was formed. The stars were formed directly out of the fragmenting disk.

2. The “inspiraling star cluster” scenario (Gerhard 2001; McMillan & Portegies Zwart 2003; Portegies Zwart et al. 2003; Kim & Morris 2003; Kim et al. 2004; Gürkan & Rasio 2005). Here the idea is that young stars were originally formed outside the hostile central parsec and only transported there later on. Individual transport of stars by two-body relaxation and mass segregation from farther out takes too long a time ( $\approx 10^{7.5}$ – $10^9$  yr; Alexander 2005). Stars in a bound, massive cluster can sink in much more rapidly owing to dynamical friction (Gerhard 2001). To sink from an initial radius of a few parsecs or more to a final radius of  $\ll 1$  pc within an O star lifetime (a few Myr) requires a cluster mass  $> 10^5 M_{\odot}$ . To prevent the final tidal disruption of such a cluster at too large a radius, resulting in the deposition of its stars there, the core of the original star cluster also has to be much denser ( $> 10^7 M_{\odot} \text{ pc}^{-3}$ ) and more compact ( $\ll 1$  pc) than any known cluster. However, as a helpful by-product, dynamical processes in such a hypothetical superdense star cluster may then lead to the formation of a central, intermediate-mass BH (IMBH; Portegies Zwart & McMillan 2002; Gürkan et al. 2004). Such a BH may help to stabilize the cluster core against tidal disruption and lessen the high-density requirement somewhat (Hansen & Milosavljevic 2003).

The “paradox of youth” in the central S star cluster, with  $> 15$  apparently normal main-sequence B stars residing in tightly bound

orbits in the central light-month around the central BH, probably requires yet another explanation (recently Ghez et al. 2003, 2005; Genzel et al. 2003; Hansen & Milosavljevic 2003; Gould & Quillen 2003; Alexander & Livio 2004; Eisenhauer et al. 2005; Alexander 2005; Davies & King 2005). Perhaps the most promising route to get the B stars into the central arcsecond is a scattering process from the reservoir of massive, young stars at  $\approx 3''$ – $10''$  (e.g., Alexander & Livio 2004).

To test these proposals, the detailed properties and dynamics of the massive stars in the central parsec must be studied. These properties include exact stellar type, spatial distribution, and three-dimensional space velocities. For this purpose, high-resolution imaging and spectroimaging are required. The new AO-assisted, near-infrared integral field spectrometer on the ESO VLT, SPIFFI/SINFONI (Eisenhauer et al. 2003a; Bonnet et al. 2004), represents a key new capability for addressing the issues discussed above. We report in this paper SPIFFI/SINFONI observations in 2003, 2004, and 2005 that give important new information on the location, dynamics, and evolution of the massive, early-type stars in the central parsec. We begin by discussing the SPIFFI/SINFONI observations and data analysis in § 2. This is followed by presentation of our results in § 3. In § 4 we discuss the implications of our findings. Further technical details are presented in the appendices.

## 2. OBSERVATIONS AND DATA ANALYSIS

### 2.1. Observations

SPIFFI (Eisenhauer et al. 2003a, 2003b) is a near-infrared integral field spectrometer providing a 2048 pixel spectrum simultaneously for a contiguous,  $64 \times 32$  pixel field. Its salient features include a reflective image slicer and a grating spectrometer with an overall detective throughput (including preoptics module and telescope) of  $\geq 30\%$ . Its  $2048^2$  pixel Hawaii II detector covers the *J*, *H*, and *K* ( $1.1$ – $2.45 \mu\text{m}$ ) atmospheric bands. In its 2003 version with a smaller  $1024^2$  pixel detector the spectrometer provided 1024 spectra for a  $32^2$  pixel field. Spectral resolving powers range from  $R = 1000$  to 4000. Three pixel scales ( $12.5 \times 25$ ,  $50 \times 100$ , and  $125 \times 250 \text{ mas}^2$ ) can be chosen on the fly. In the SINFONI ESO VLT facility, SPIFFI is mated with the MACAO AO module (Bonnet et al. 2003) employing a 60-element wave front curvature sensor with avalanche photodiodes. This mode makes it possible to perform spectroscopy at the smallest (diffraction limited) pixel scale.

Table 1 lists the various data sets we have been able to obtain with both SPIFFI as a guest instrument (in 2003) and SINFONI during its commissioning in 2004 and guaranteed time observation (GTO) runs in 2005. These data have been taken in the *K* band with a resolution  $R = 4000$  ( $\text{FWHM} = 85 \text{ km s}^{-1}$ ) and in the *H+K* mode ( $R = 1500$ ,  $\text{FWHM} = 230 \text{ km s}^{-1}$ ). Preliminary results from the 2003 seeing-limited data sets were presented in Genzel et al. (2003), Horrobin et al. (2004), and Paumard et al. (2004a)<sup>14</sup>. The 2004 mosaic supersedes the 2003 *K*-band one. Although the FWHM resolution of these two sets is almost identical, the AO reduced dramatically the wings of the point-spread function (PSF), rendering unnecessary the complex method for correction of the nebular emission described in Paumard et al. (2004a). Figure 1 shows the coverage of these spectral cubes, superposed on a diffraction-limited *L'*-band ( $3.76 \mu\text{m}$ ) image taken with the adaptive optics assisted near-IR imager and spectrograph NACO on ESO VLT (Lenzen et al. 2003; Rousset et al. 2003).

We also analyzed several high-quality *H*- and *K<sub>s</sub>*-band, diffraction-limited images taken during 2002–2004 with NACO during our

<sup>14</sup> See also [http://www-laog.obs.ujf-grenoble.fr/ylu/ylu\\_vgr/vgr\\_index.html](http://www-laog.obs.ujf-grenoble.fr/ylu/ylu_vgr/vgr_index.html).

TABLE 1  
SUMMARY OF SPIFFI/SINFONI DATA SETS

Date	Band	Two-dimensional			Comments
		Pixel (mas)	Resolution (mas)	Mosaic Size <sup>a</sup> (arcsec)	
2003 Apr 8–9 .....	<i>K</i>	100	250	10 × 10	Excellent seeing
	<i>H+K</i>	250	900	38 × 32	...
2004 Aug 18–19 .....	<i>K</i>	100	220	10 × 10	...
2005 Mar 14–23 .....	<i>K</i>	100	200	6 × 16	Centered $\simeq 15''$ north of Sgr A* <sup>*</sup> ; very deep spectroscopy ( $m_{K, \text{lim}} \simeq 16-17.5$ )
	<i>K</i>	100	200	4 × 20	Long dimension southwest-northeast; centered $\simeq 15''$ northeast of Sgr A* <sup>*</sup>
2005 Jun 17 .....	<i>K</i>	250	1000	40 × 40	“Frame” completing 2003 <i>H+K</i> mosaic

<sup>a</sup> Unless otherwise specified, east-west × north-south.

GTO astrometry imaging program to construct very deep images of the IRS 13E and IRS 16 regions. We return to this when we discuss these images in § 3.3.

### 2.2. Spectral Identification of Early-Type Stars

Interpretation of stellar spectra in the GC is hindered by stellar crowding and ionized interstellar gas emission, especially in H I 2.166  $\mu\text{m}$  (Br $\gamma$ ) and He I 2.058  $\mu\text{m}$ . As a result, previous seeing-limited spectroscopic observations have relatively easily detected broad emission line stars, such as W-R stars and other evolved objects (Ofpe/WN stars), but have not been successful in detecting near-main-sequence OB stars. These are characterized by relatively weak absorption features of He I (2.058, 2.113, 2.163  $\mu\text{m}$ ) and H I Br $\gamma$  (Hanson et al. 2005; the feature at 2.113  $\mu\text{m}$  is in fact a compound of four He I lines and three N III lines). The new high-resolution SINFONI data overcome both of these issues to a considerable extent. We can now reliably detect all OB supergiants

and giants ( $m_K \simeq 11-13$ ). In less crowded regions without strong nebular emission we are now also successful in detecting OB main-sequence stars ( $m_K \simeq 13-15$ ; see also Eisenhauer et al. 2005).

We searched for OB stars by visual inspection of two-dimensional continuum-subtracted line maps in the above-mentioned lines. Br $\gamma$  and He I 2.058  $\mu\text{m}$  are usually intrinsically stronger than He I 2.113  $\mu\text{m}$ , but the latter does not suffer from the problem of nebular emission. This line is, therefore, a good choice for identification of OB stars, especially in the lower resolution *H+K* data. The spectra of the OB candidates so identified were then extracted with the interstellar emission removed by subtracting an off-source spectrum (generally from a ring around each source).

For the medium plate scale ( $50 \times 100 \text{ mas}^2 \text{ pixel}^{-1}$ ) *K*-band data, the diffuse emission can in most cases be successfully removed by this subtraction. The correction is not perfect, especially for stars embedded in the interstellar medium, which they excite locally. In other cases the profiles of the interstellar emission are complex and vary rapidly from position to position (Paumard et al. 2004b). As a result, there remain considerable uncertainties around Br $\gamma$  and He I 2.058  $\mu\text{m}$  in the spectra extracted near/on minispiral streamers. In a few cases, especially for fainter stars, the spectral identification of the stars is not certain. We have taken these issues into account by grouping stars into three quality codes. Stars with code 2 have high-quality spectra and certain identification. Stars with code 1 have possible uncertainties in the extraction of some of the key spectral features. In the case of stars with code 0 the identification (as early-type stars) is preliminary and needs to be confirmed. For a positive identification of a candidate Br $\gamma$  absorption line star we require that the stellar spectrum does not exhibit any signs for the 2.3–2.4  $\mu\text{m}$  CO overtone absorption bands characteristic of late-type stars.

In the larger *K* and *H+K* cubes at lower spectral and spatial resolution (the outer square and rectangles in Fig. 1), the nebular emission subtraction becomes much harder. There remains only the possibility of looking for the He I/N III complex at 2.113  $\mu\text{m}$  as explained above, but the cube in this case is filled with an unresolved background of late-type stars: the CO break at 2.29  $\mu\text{m}$ , which is obvious in almost every pixel in the field, cannot be used as a discriminator. All spectra are contaminated to some extent by the numerous absorption lines that the cool stars exhibit (Wallace & Hinkle [1997] speak of a “grass” of absorption lines). We see in particular Al I 2.1099, 2.1132, and 2.1170  $\mu\text{m}$ . This makes the identification of He I 2.1127  $\mu\text{m}$  uncertain or even doubtful. While we find many emission-line stars in this cube, we regard the identification of a number of absorption-line stars as reasonably safe and classify them with the same quality codes.

To obtain stellar identifications, we compared the extracted spectra with templates from the literature. For the wind-dominated

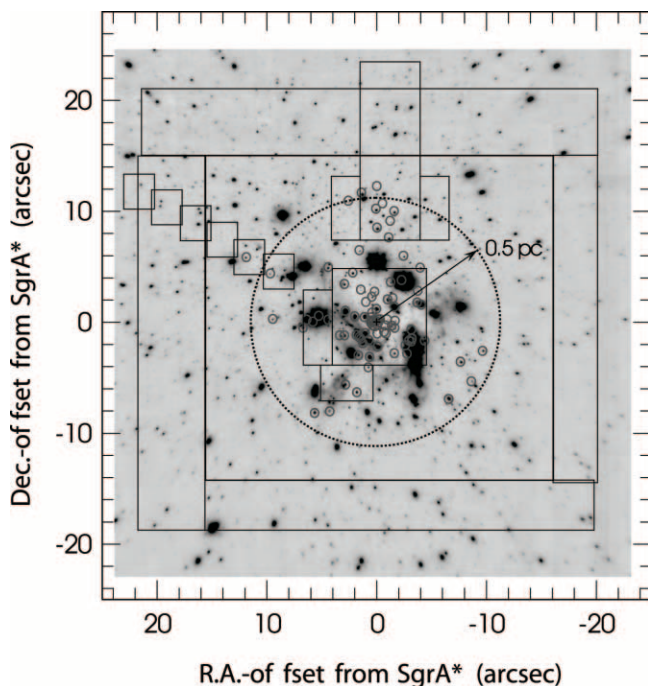


FIG. 1.—Outline of the various 2003–2005 SPIFFI/SINFONI *H+K*- and *K*-band cubes, superposed on a  $\simeq 100$  mas resolution, *L*-band NACO image (logarithmic scale). Small circles denote the 90 quality 1 and 2 early-type stars (OB I–V, Ofpe/WN9, W-R stars) reported in this paper (Table 2). A dotted circle denotes a 0.5 pc radius zone centered on Sgr A\*<sup>\*</sup>, within which essentially all OB stars we have found appear to lie. [See the electronic edition of the *Journal* for a color version of this figure.]

stars and W-R stars we mainly used the atlas of Morris et al. (1996) and Figer et al. (1997). For the OB stars we referred to Hanson et al. (1996, 2005). We compared spectra from the latter atlas individually to the GC stars and made spectral identifications based on the strength of the He I, H I, He II, and N III lines, along with equivalent widths and line profiles/widths. We computed absolute magnitudes from the observed magnitudes and individual extinction corrections (Appendix F). These absolute  $K$  magnitudes are used in our final classifications (Table 2) as an additional constraint for placing the stars in the different luminosity classes.

### 2.3. Determination of Velocities

For the emission-line stars we deduced stellar radial velocities using a variety of techniques. We fitted simple Gaussian profiles wherever possible and averaged values obtained from different lines, giving larger weight to single transitions. For lines with P Cyg profiles we fitted a combination of an emission and an absorption line. We also constructed template spectra for well-identified W-R, Ofpe/WN9, and LBV profiles, either from the GC stars themselves or from the literature (Figer et al. 1997). Velocities were then obtained from cross-correlation. For those stars for which velocities are available in the literature (Genzel et al. 2000, 2003; Paumard et al. 2001; Najarro et al. 1994, 1997), we averaged our results with the earlier values. In the analysis of Najarro et al. (1994, 1997) the stellar velocity was a fit parameter in an overall radiative transport, stellar atmosphere model of the line profiles. Overall we find that for the wind-dominated stars the accuracy of velocity determinations is dominated by the large velocity widths and complex line profiles. In a few cases where we have line profiles over a number of years, we find some evidence for variability in the line profiles. The  $1\sigma$  uncertainties of the velocities are typically  $\pm 50$ – $100\text{ km s}^{-1}$ .

The situation is much more straightforward for the new OB supergiants, giants, and main-sequence stars. In this case we are dealing mostly with optically thin absorption lines of well-determined transitions and with simple line profiles. An exception is the vicinity of H I Br $\gamma$  for the OB supergiants and giants. In these cases the line profiles clearly show evidence for He I 7–4, which is a complex of seven transitions between  $-80$  and  $-1000\text{ km s}^{-1}$  blueward of H I 7–4 (Najarro et al. 1994). The relative strengths of He I 7–4 and H I 7–4 are abundance and atmosphere dependent and need to be treated as free parameters. As a result of this fairly simple situation, the  $1\sigma$  accuracy of velocity determinations is mainly limited by signal-to-noise ratio and line width and can be as good as  $\pm 20\text{ km s}^{-1}$ .

## 3. RESULTS

### 3.1. OB Stars Are Finally Detected

Our observations have led to the firm detection of 29 OB supergiants (luminosity class I–II), as well as 12 OB stars of luminosity class III and V. They are listed in Table 2 as quality 1 and 2. In addition, we have 18 OB candidates whose identifications we regard as tentative (quality 0; Table 3). Those additional stars need to be confirmed. All of these detections refer to the region outside the central cusp, with projected radius  $p_{\text{Sgr A}^*} \geq 0''.8$ . Eisenhauer et al. (2005) have already reported 70 mas resolution SINFONI observations of this central cusp, with the detection of more than a dozen main-sequence B stars, in addition to the late O9/B0 main-sequence star S2 (S02) detected earlier by Ghez et al. (2003). For completeness, these S stars are listed as the first 14 entries in Table 2.

Figure 2 shows the co-added spectra of the 10 best OB I stars and the nine best O III/V stars. A comparison with the atlas of

Hanson et al. (2005) shows that these two sample average spectra are very similar to their respective solar neighborhood templates. After more than a decade of search, our data finally reveal the missing OB population in the GC. It is clear that the non-detection of these stars in earlier studies was merely an instrumental effect.

In addition to the 41 new OB stars outside the central  $0''.85$ , we identify 30 post-main-sequence blue supergiants and Wolf-Rayet stars, adding several stars to the sample already known from previous work (Genzel et al. 1996, 2000, 2003; Paumard et al. 2001). Of these, we classify 17 as Ofpe/WN9 and late nitrogen-rich W-R (WNL=WN7–9) stars and 12 as carbon-rich W-R (WC) stars. There is one early WN (WNE, WN5/6) star, IRS 16SE2. The northern arm bow shock star IRS 1W, with Br $\gamma$  in emission and He I  $\lambda$  2.058  $\mu\text{m}$  in absorption as the only features, is perhaps a Be star (for spectrum and detailed discussion see Paumard et al. 2004a). There is also one additional tentative WC candidate (IRS 7SE2).

Tanner et al. (2006) classify the six bright Ofpe/WN9 stars (narrow emission line stars and LBV candidates from Paumard et al. 2001) as B stars on the basis that they do not detect N III 2.116  $\mu\text{m}$  emission in these stars. They also do not detect the He I complex at 2.113  $\mu\text{m}$  for the variable star and best LBV candidate IRS 34W (Trippe et al. 2006), in contrast to the other five. However, we clearly detect these features although the He I feature is mostly in emission (with some P Cyg absorption) in IRS 34W (see spectra in Paumard et al. 2004a; Trippe et al. 2006).

Hanson et al. (1996) have suggested that these very bright stars in the IRS 16 cluster might be OBN stars. OBN stars are particular kinds of O and B stars that show unusually strong N lines in the optical. They are also known to show unusually strong He lines and to be particularly bright because of a lower atmospheric opacity (Langer 1992). Indeed, the strengths of the 2.115  $\mu\text{m}$  N III compound and the 2.163  $\mu\text{m}$  He I 7–4 absorption, relative to Br $\gamma$ , in the average spectrum of the newly detected supergiants in Figure 2 suggest that many of the luminous OB stars in the central parsec are nitrogen- and helium-rich. An extreme case is IRS 16CC, where the He I absorption line at 2.163  $\mu\text{m}$  is almost as deep as the Br $\gamma$  line. The only stars of the Hanson et al. (1996, 2005) atlases to show comparable depth in He I 2.163  $\mu\text{m}$  are HD 191781 and HD 123008, two ON9.7 Iab stars. Detailed modeling of our new stars is ongoing (F. Martins et al. 2006, in preparation). Preliminary results seem to confirm a He enrichment (He/H  $\simeq 0.3 \pm 0.1$ ) for the “average” star. This is still compatible with standard evolutionary models with rotation, however. Based on simple morphological arguments, the stronger absorption in He I 2.163  $\mu\text{m}$  in IRS 16CC and IRS 16SSE2 may indicate an even larger helium enrichment, which could be in conflict with theoretical predictions. More work is definitely needed to draw any reliable conclusion.

All of these evolved stars are included in Tables 2 and 3. In total, Table 2 lists 90 certain detections of early-type stars. Table 3 has an additional 14 further candidates. More than 100 early-type stars have now been detected in the nuclear star cluster, and this number is expected to grow in the next years.

### 3.2. Dynamics of the Young Stars

#### 3.2.1. Two Disks of Early-Type Stars

Genzel et al. (1996) were the first to note that the 20 or so bright “He I” emission line stars between  $p = 1''$  and  $12''$  known at that time exhibit a coherent rotation pattern in their radial velocities. Stars north of the center are blueshifted, while stars south of the center are redshifted. This pattern is opposite to Galactic rotation. Genzel et al. (2000) and Paumard et al. (2001)

TABLE 2  
 PROPERTIES OF EARLY-TYPE STARS (QUALITY 1+2) IN THE CENTRAL PARSEC

Name	$p$ (arcsec)	$x$ (arcsec)	$y$ (arcsec)	$z$ (arcsec)	$m_K$	$v_x$ (km s <sup>-1</sup> )	$v_y$ (km s <sup>-1</sup> )	$v_z$ (km s <sup>-1</sup> )	$j$	$e^a$	Type	$Q$	$M_K$
E1: S2, S02.....	0.12	0.04	0.12	...	14.0	9 ± 32	1830 ± 43	-1060 ± 25	0.29 ± 0.02	0.876 ± 0.007	B0-2 V	2	-3.9 ± 0.6
E2: S14, S016.....	0.14	0.12	0.07	...	15.7	2106 ± 191	1103 ± 88	300 ± 80	-0.04 ± 0.05	0.939 ± 0.008	B4-9 V	2	-2.2 ± 0.6
E3: S13, S020.....	0.16	-0.16	0.00	...	15.8	359 ± 93	1483 ± 52	-280 ± 50	-0.98 ± 0.03	0.395 ± 0.032	B4-9 V	2	-2.1 ± 0.6
E4: S1, S01.....	0.21	-0.04	-0.20	...	14.5	801 ± 28	-1183 ± 44	-1033 ± 25	0.71 ± 0.02	0.358 ± 0.036	B0-2 V	2	-3.4 ± 0.6
E5: S12, S019.....	0.23	-0.06	0.26	...	15.5	255 ± 79	1098 ± 56	280 ± 50	-0.46 ± 0.07	0.902 ± 0.005	B4-9 V	2	-2.4 ± 0.6
E6: S4, S03.....	0.29	0.26	0.11	...	14.4	623 ± 26	74 ± 24	-570 ± 40	-0.28 ± 0.04	...	B0-2 V	2	-3.5 ± 0.6
E7: S08.....	0.40	-0.30	0.27	...	15.8	121 ± 23	-471 ± 21	-390 ± 70	0.54 ± 0.04	...	B4-9 V	2	-2.1 ± 0.6
E8: S5.....	0.40	0.36	0.17	...	15.0	-134 ± 30	355 ± 30	30 ± 90	1.00 ± 0.08	...	B4-9 V	2	-2.9 ± 0.6
E9: S9, S05.....	0.40	0.18	-0.36	...	15.1	109 ± 23	-499 ± 23	610 ± 40	-0.26 ± 0.05	...	B0-2 V	2	-2.8 ± 0.6
E10: S8, S04.....	0.45	0.37	-0.26	...	14.5	536 ± 45	-569 ± 41	15 ± 30	-0.21 ± 0.05	0.927 ± 0.019	B0-2 V	2	-3.4 ± 0.6
E11: S6, S07.....	0.48	0.47	0.09	...	15.4	295 ± 30	-21 ± 24	160 ± 60	-0.25 ± 0.08	...	B V	2	-2.5 ± 0.6
E12: S7, S011.....	0.53	0.53	-0.05	...	15.2	-225 ± 22	-93 ± 23	-20 ± 150	-0.46 ± 0.10	...	B V	2	-2.7 ± 0.6
E13.....	0.68	0.53	0.43	...	15.1	153 ± 23	-20 ± 22	-890 ± 31	-0.73 ± 0.15	...	B V	2	-2.8 ± 0.6
E14: S014.....	0.82	-0.78	-0.28	...	13.7	34 ± 21	-2 ± 20	-14 ± 40	0.39 ± 0.60	...	O9.5-B2 V	2	-3.9 ± 0.6
E15: S1-3.....	0.96	0.43	0.86	1.57 ± 0.33	12.2	-518 ± 21	115 ± 22	68 ± 40	0.97 ± 0.04	0.000 ± 0.151	?	2	-4.9 ± 1.1
E16: S015.....	0.98	-0.94	0.26	0.22 ± 0.24	13.6	-262 ± 23	-374 ± 26	-424 ± 70	0.94 ± 0.06	0.096 ± 0.173	O9-9.5 V	2	-3.4 ± 0.9
E17.....	1.01	-0.04	-1.01	-1.70 ± 0.48	14.7	432 ± 29	8 ± 28	26 ± 30	1.00 ± 0.07	0.107 ± 0.255	?	1	-3.0 ± 0.5
E18: [GEO97] W11 <sup>b</sup> .....	1.09	-0.66	-0.87	-1.96 ± 0.56	14.1	313 ± 28	-144 ± 28	-364 ± 40	0.98 ± 0.08	0.636 ± 0.229	OB	1	-3.6 ± 0.5
E19: IRS 16NW.....	1.21	0.03	1.21	...	10.0	199 ± 52	67 ± 44	-44 ± 20	-0.94 ± 0.25	0.898 ± 0.052	Ofpe/WN9	2	-7.4 ± 0.4
E20: IRS 16C.....	1.23	1.13	0.48	1.22 ± 0.46	9.7	-342 ± 50	302 ± 44	125 ± 30	0.90 ± 0.10	0.075 ± 0.279	Ofpe/WN9	2	-6.7 ± 0.4
E21: [GEO97] W13 <sup>b</sup> .....	1.31	-0.85	-1.00	-1.91 ± 0.45	13.8	397 ± 28	-65 ± 27	-24 ± 30	0.86 ± 0.07	0.349 ± 0.159	OB I?	2	-3.9 ± 0.7
E22: [GEO97] W10 <sup>b</sup> .....	1.40	-1.36	-0.31	-0.90 ± 0.33	12.8	157 ± 29	-277 ± 27	-434 ± 50	0.96 ± 0.08	0.204 ± 0.219	O8-9.5 III/I	2	-4.2 ± 0.6
E23: IRS 16SW.....	1.43	1.05	-0.98	-1.46 ± 0.51	9.9	261 ± 47	90 ± 43	320 ± 40	0.88 ± 0.16	0.410 ± 0.190	Ofpe/WN9	2	-6.5 ± 0.4
E24: [GEO97] W7 <sup>b</sup> .....	1.68	-1.67	0.14	-0.21 ± 0.38	13.1	62 ± 29	-206 ± 28	-344 ± 50	0.93 ± 0.13	0.413 ± 0.177	O9-9.5 III?	2	-4.5 ± 0.5
E25: [GEO97] W14 <sup>b</sup> .....	1.72	-1.64	-0.50	-1.15 ± 0.66	12.7	273 ± 28	-81 ± 28	-224 ± 50	0.55 ± 0.10	...	O8.5-9.5 I?	2	-4.2 ± 0.5
E26: IRS 16SSW.....	1.75	0.72	-1.60	...	11.5	118 ± 28	-207 ± 29	206 ± 30	0.10 ± 0.12	...	O8-9.5 I	2	-5.5 ± 0.5
E27: IRS 16CC.....	2.08	2.01	0.54	1.35 ± 0.54	10.4	-85 ± 44	219 ± 45	241 ± 25	0.99 ± 0.19	0.478 ± 0.137	O9.5-B0.5 I	2	-6.7 ± 1.1
E28: IRS 16SSE2.....	2.08	1.45	-1.49	-2.13 ± 0.54	12.4	292 ± 28	120 ± 27	286 ± 20	0.93 ± 0.09	0.228 ± 0.241	B0-0.5 I	2	-4.4 ± 0.4
E29.....	2.08	0.99	1.83	3.21 ± 0.57	13.7	-254 ± 28	67 ± 27	-94 ± 50	0.97 ± 0.11	0.490 ± 0.170	O9-B0	2	-3.5 ± 0.8
E30: IRS 16SSE1.....	2.09	1.59	-1.36	-1.85 ± 0.57	12.2	291 ± 29	116 ± 28	216 ± 20	0.88 ± 0.09	0.057 ± 0.212	O8.5-9.5 I	2	-4.9 ± 0.5
E31: IRS 29N.....	2.14	-1.60	1.41	...	10.0	130 ± 50	-119 ± 45	-190 ± 90	0.02 ± 0.27	...	WC9	2	-7.7 ± 0.4
E32: MPE+1.6-6.8(16SE1).....	2.18	1.85	-1.15	-1.52 ± 0.63	10.9	184 ± 43	124 ± 44	366 ± 70	0.91 ± 0.20	0.260 ± 0.347	WC8/9	2	-5.9 ± 0.5
E33: IRS 33N.....	2.19	-0.06	-2.19	...	11.1	85 ± 30	-212 ± 40	68 ± 20	0.40 ± 0.16	...	B0.5-1 I	2	-5.8 ± 0.4
E34: MPE+1.0-7.4(16S).....	2.26	1.27	-1.88	-2.70 ± 0.61	10.7	301 ± 47	1 ± 43	100 ± 20	0.83 ± 0.15	0.100 ± 0.287	B0.5-1 I	2	-6.1 ± 0.6
E35: IRS 29NE1.....	2.28	-0.99	2.06	2.99 ± 0.60	11.7	-370 ± 51	25 ± 43	-100 ± 70	0.87 ± 0.13	0.140 ± 0.306	WC8/9	2	-6.0 ± 0.4
E36.....	2.34	0.45	2.29	3.52 ± 0.56	12.5	-317 ± 29	85 ± 27	41 ± 20	1.00 ± 0.09	0.192 ± 0.121	O9-B0 I?	2	-5.3 ± 0.4
E37.....	2.62	-1.47	2.17	...	14.8	130 ± 29	-143 ± 28	-114 ± 30	-0.14 ± 0.15	...	O8-9 I?	2	-3.3 ± 0.5
E38.....	2.76	0.19	2.76	3.47 ± 0.54	13.1	-342 ± 46	85 ± 43	36 ± 20	0.98 ± 0.13	0.279 ± 0.166	O8-9 III/I	2	-5.0 ± 0.5
E39: IRS 16NE.....	3.05	2.87	1.03	...	8.9	104 ± 49	-379 ± 47	-10 ± 20	-1.00 ± 0.12	0.000 ± 0.234	Ofpe/WN9	2	-7.5 ± 0.6
E40: IRS 16SE2.....	3.17	2.94	-1.19	-1.20 ± 0.71	12.0	107 ± 28	181 ± 29	327 ± 100	0.99 ± 0.14	0.206 ± 0.288	WN5/6	2	-4.5 ± 0.4
E41: IRS 33E.....	3.19	0.65	-3.12	-3.57 ± 0.50	10.1	182 ± 47	-9 ± 42	170 ± 20	0.97 ± 0.26	0.630 ± 0.186	Ofpe/WN9	2	-6.3 ± 0.4
E42.....	3.20	-3.13	-0.66	...	14.6	-52 ± 28	257 ± 28	40 ± 40	-1.00 ± 0.10	0.358 ± 0.218	B V/III	2	-2.7 ± 0.6
E43.....	3.21	-1.60	-2.79	-3.57 ± 0.50	12.2	227 ± 29	1 ± 28	-114 ± 50	0.87 ± 0.13	0.214 ± 0.297	O8.5-9.5 I	2	-4.7 ± 0.4
E44.....	3.29	1.45	2.95	3.63 ± 0.42	13.8	-259 ± 29	53 ± 27	-114 ± 40	0.97 ± 0.11	0.508 ± 0.164	O9-B0 II/I?	2	-4.1 ± 0.5
E45.....	3.33	-2.61	-2.08	...	12.5	175 ± 27	106 ± 28	63 ± 30	0.13 ± 0.13	...	O9-B0 I	2	-4.3 ± 0.4
E46: IRS 13E1.....	3.37	-2.94	-1.64	...	10.7	-201 ± 45	-50 ± 42	71 ± 20	-0.26 ± 0.21	...	B0-1 I	2	-5.6 ± 0.3
E47.....	3.41	1.67	-2.97	...	12.5	-49 ± 25	150 ± 25	91 ± 30	0.20 ± 0.16	...	B0-3 I	2	-4.4 ± 0.4
E48: IRS 13E4.....	3.50	-3.19	-1.42	...	11.7	-316 ± 29	76 ± 29	56 ± 70	-0.61 ± 0.09	0.809 ± 0.058	WC9	2	-4.7 ± 0.4
E49: IRS 13E3 <sup>c</sup> .....	3.53	-3.19	-1.51	...	13.0	-157 ± 29	118 ± 30	87 ± 20	-0.88 ± 0.15	0.725 ± 0.098	?	2	-5.2 ± 0.3
E50: IRS 16SE3.....	3.54	3.35	-1.16	-0.93 ± 0.76	11.9	7 ± 29	201 ± 27	281 ± 20	0.96 ± 0.14	0.319 ± 0.224	O8.5-9.5 I	2	-4.7 ± 0.6

TABLE 2—Continued

Name	$p$ (arcsec)	$x$ (arcsec)	$y$ (arcsec)	$z$ (arcsec)	$m_K$	$v_x$ (km s <sup>-1</sup> )	$v_y$ (km s <sup>-1</sup> )	$v_z$ (km s <sup>-1</sup> )	$j$	$e^a$	Type	$Q$	$M_K$
E51: IRS 13E2.....	3.59	-3.14	-1.74	...	10.8	-303 ± 44	68 ± 46	40 ± 40	-0.66 ± 0.15	0.749 ± 0.099	WN8	2	-5.6 ± 0.4
E52.....	3.84	-1.26	3.62	...	13.3	214 ± 28	214 ± 26	-167 ± 20	-0.90 ± 0.09	0.378 ± 0.183	O8-9 III	2	-4.8 ± 0.4
E53.....	3.95	-2.76	-2.83	...	12.4	-65 ± 25	-154 ± 25	29 ± 20	0.36 ± 0.15	...	B0-1 I	2	-4.7 ± 0.6
E54: IRS 34E.....	4.08	-3.67	1.80	2.12 ± 0.88	12.6	-221 ± 28	-131 ± 27	-154 ± 25	0.84 ± 0.10	0.171 ± 0.215	O9-9.5 I	2	-5.0 ± 0.6
E55.....	4.14	0.77	-4.06	...	12.5	-65 ± 29	-159 ± 27	76 ± 20	-0.54 ± 0.17	...	B0-1 I?	2	-4.3 ± 0.4
E56: IRS 34W.....	4.35	-4.05	1.59	1.55 ± 0.89	11.4	-79 ± 28	-166 ± 27	-290 ± 30	1.00 ± 0.15	0.217 ± 0.354	Ofpe/WN9	2	-5.8 ± 0.5
E57.....	4.43	4.42	0.25	1.48 ± 0.96	13.5	-109 ± 28	114 ± 27	196 ± 40	0.76 ± 0.17	0.343 ± 0.260	O7-9 III?	2	-3.0 ± 0.5
E58: IRS 3E.....	4.48	-2.26	3.80	...	15.0	...	...	107 ± 100	...	...	WC5/6	1	-2.9 ± 0.6
E59: [PMM2001] B9 <sup>b</sup> .....	4.54	2.94	3.46	...	13.0	250 ± 28	32 ± 26	-150 ± 100	-0.67 ± 0.11	0.794 ± 0.078	WC9	2	-4.0 ± 0.6
E60.....	4.66	-4.36	-1.65	...	12.4	-210 ± 27	127 ± 27	330 ± 80	-0.79 ± 0.11	1.046 ± 0.311	WN7?	2	-4.5 ± 0.6
E61: IRS 34NW.....	4.69	-3.73	2.85	3.08 ± 0.81	12.8	-225 ± 28	-112 ± 27	-150 ± 30	0.90 ± 0.11	0.000 ± 0.230	WN7	2	-4.6 ± 0.6
E62.....	4.99	2.18	4.48	...	11.5	229 ± 42	-66 ± 43	-134 ± 40	-0.99 ± 0.18	0.325 ± 0.229	B0-3 I	2	-6.5 ± 0.5
E63: IRS 1W.....	5.30	5.27	0.57	...	9.6	-108 ± 44	209 ± 55	35 ± 20	0.93 ± 0.23	0.410 ± 0.304	Be?	1	-7.1 ± 0.3
E64.....	5.81	5.81	0.05	...	12.4	-20 ± 30	170 ± 25	40 ± 25	0.99 ± 0.15	0.572 ± 0.151	O9.5-B2 II	2	-4.4 ± 0.4
E65: IRS 9W.....	6.30	2.85	-5.62	...	12.1	167 ± 29	135 ± 27	140 ± 50	0.98 ± 0.13	0.665 ± 0.242	WN8	2	-4.1 ± 0.4
E66: IRS 7SW.....	6.32	-3.95	4.93	...	12.0	-5 ± 27	-108 ± 26	-350 ± 50	0.66 ± 0.25	1.261 ± 0.216	WN8	2	-4.4 ± 0.5
E67: IRS 1E.....	6.38	6.37	0.23	...	11.2	-107 ± 43	136 ± 49	8 ± 20	0.81 ± 0.28	0.701 ± 0.232	B1-3 I	2	-5.6 ± 0.4
E68: IRS 7W.....	6.47	-2.45	5.99	...	13.1	185 ± 29	36 ± 28	-305 ± 100	-0.98 ± 0.15	0.155 ± 0.583	WC9	2	-4.6 ± 0.4
E69.....	6.58	1.81	-6.32	...	11.1	202 ± 29	91 ± 28	153 ± 50	0.99 ± 0.13	0.791 ± 0.359	?	1	-5.5 ± 0.6
E70: IRS 7E2(ESE).....	6.64	4.41	4.97	...	12.9	203 ± 28	-7 ± 26	-80 ± 100	-0.77 ± 0.13	0.714 ± 0.104	Ofpe/WN9	2	-4.1 ± 0.5
E71.....	6.68	1.59	6.49	...	14.1	-148 ± 30	189 ± 29	-300 ± 150	0.79 ± 0.13	0.730 ± 0.284	WC8/9?	1	-3.8 ± 0.6
E72.....	6.73	6.71	-0.50	...	13.6	65 ± 28	100 ± 28	86 ± 100	0.87 ± 0.24	0.555 ± 0.243	WC9?	2	-3.0 ± 0.3
E73.....	7.73	-1.08	7.65	...	11.5	-160 ± 50	22 ± 50	-92 ± 40	0.96 ± 0.31	0.373 ± 0.353	O9-B I	2	-5.1 ± 0.3
E74: AFNW.....	8.42	-7.63	-3.57	...	11.7	-67 ± 28	-92 ± 28	70 ± 70	0.48 ± 0.25	0.932 ± 0.055	WN8	2	-4.5 ± 0.4
E75.....	8.53	-0.02	8.53	...	11.0	-35 ± 45	226 ± 40	-138 ± 40	0.15 ± 0.20	0.727 ± 0.405	O9-B I	2	-5.8 ± 0.5
E76: IRS 9SW.....	9.10	4.28	-8.03	...	13.1	108 ± 49	8 ± 45	180 ± 80	0.91 ± 0.45	0.521 ± 0.374	WC9	2	-3.4 ± 0.3
E77.....	9.23	-1.23	9.15	...	13.6	...	...	-155 ± 50	...	...	O9-B0 V	2	-3.3 ± 0.6
E78: [PMM2001] B1 <sup>b</sup> .....	9.47	9.46	0.31	...	13.0	-161 ± 46	-142 ± 55	-230 ± 100	-0.64 ± 0.26	0.781 ± 0.216	WC9	2	-3.4 ± 0.6
E79: AF.....	9.51	-6.54	-6.91	...	10.8	68 ± 36	50 ± 36	160 ± 30	0.18 ± 0.43	0.991 ± 0.016	Ofpe/WN9	2	-5.7 ± 0.8
E80: IRS 9SE.....	9.93	5.65	-8.17	...	11.7	-2 ± 36	-131 ± 36	130 ± 100	-0.58 ± 0.28	0.766 ± 0.181	WC9	2	-5.2 ± 0.6
E81: AFNWNW.....	9.97	-9.63	-2.58	...	12.6	87 ± 31	-9 ± 38	30 ± 70	0.36 ± 0.43	0.873 ± 0.115	WN7	2	-4.9 ± 0.9
E82: Blum.....	10.14	-8.63	-5.33	...	13.0	-53 ± 34	249 ± 46	-70 ± 70	-0.94 ± 0.17	0.646 ± 0.467	WC8/9	2	-3.7 ± 0.8
E83: IRS 15SW.....	10.15	-1.58	10.02	...	12.0	-55 ± 39	-32 ± 38	-180 ± 70	0.93 ± 0.62	0.863 ± 0.135	WN8/WC9	2	-5.5 ± 0.4
E84.....	10.24	0.08	10.24	...	11.3	-119 ± 42	74 ± 42	-250 ± 40	0.85 ± 0.30	...	O9-B I	2	-6.2 ± 0.5
E85.....	10.63	9.68	4.39	...	12.8	...	...	-150 ± 40	...	...	OB	2	-3.7 ± 0.4
E86.....	10.71	-0.53	10.72	...	15.0	93 ± 39	73 ± 40	-205 ± 50	-0.82 ± 0.32	0.684 ± 0.434	OB V?	2	-1.6 ± 0.4
E87.....	11.25	2.58	10.94	...	13.7	-88 ± 39	-82 ± 37	-120 ± 30	0.56 ± 0.32	0.933 ± 0.072	B V/III	2	-3.5 ± 0.8
E88: IRS 15NE.....	11.76	1.38	11.68	...	11.8	-8 ± 39	103 ± 46	-65 ± 40	0.19 ± 0.37	0.877 ± 0.114	WN8/9	2	-5.5 ± 0.5
E89.....	12.27	0.00	12.27	...	14.5	108 ± 40	17 ± 35	-100 ± 40	-0.99 ± 0.37	0.360 ± 0.314	B1-3 V	2	-2.9 ± 0.6
E90.....	13.24	11.87	5.86	...	12.1	...	...	-190 ± 40	...	...	O9-B1 I?	2	-4.5 ± 0.4

NOTES.—Errors are 1  $\sigma$  uncertainties. These columns give the following in order: name(s) of the star; projected distance to Sgr\*; three-dimensional position ( $z$  is derived by Beloborodov et al. 2006); apparent  $K$  magnitude; three-dimensional velocity; sky-projected angular momentum  $j$  (eq. [B1]); eccentricity (see Appendix C); stellar type; quality (2=highest, 1=good); and absolute  $K$  magnitude.  $M_K$  and  $e$  (except for E1–E10) assume  $R_0 = 7.62 \pm 0.32$  kpc. Parameters  $p$ ,  $x$ ,  $y$ , and  $z$  are in (equivalent) arcseconds. All velocities are in km s<sup>-1</sup>, assuming  $R_0 = 8$  kpc for  $v_x$  and  $v_y$ . Table 2 is also available in machine-readable form in the electronic edition of the *Astrophysical Journal*.

<sup>a</sup> For stars E1–E10, we quote Eisenhauer et al. (2005).

<sup>b</sup> Designation from Genzel et al. (1997, [GEO97]) or Paumard et al. (2001, [PPM2001]).

<sup>c</sup> Cluster core (multiple object).

TABLE 3  
 PROPERTIES OF CANDIDATE EARLY-TYPE STARS (QUALITY 0) IN THE CENTRAL PARSEC

Name	$\rho$	$x$	$y$	$m_K$	$v_x$	$v_y$	$v_z$	$j$	Type
S1-1 .....	1.01	1.01	0.02	13.2	$223 \pm 22$	$73 \pm 22$	?	$0.29 \pm 0.09$	E?
	1.05	-0.31	-1.00	16.0	$-348 \pm 28$	$-341 \pm 27$	?	$-0.47 \pm 0.06$	E?
	1.05	0.79	-0.69	12.5	$429 \pm 29$	$137 \pm 29$	?	$0.86 \pm 0.06$	E?
	1.12	-0.97	0.56	15.6	$-40 \pm 28$	$-88 \pm 28$	?	$1.00 \pm 0.29$	E?
	1.47	-0.55	-1.37	15.5	$-16 \pm 28$	$-28 \pm 28$	?	$-0.14 \pm 0.87$	E?
	1.65	0.37	-1.61	13.8	$281 \pm 29$	$-131 \pm 30$	$217 \pm 60$	$0.79 \pm 0.09$	OB III?
	2.34	2.32	-0.26	12.9	$-30 \pm 28$	$227 \pm 28$	$49 \pm 20$	$0.97 \pm 0.12$	OB?
	4.85	-4.11	-2.58	16.2	$-53 \pm 28$	$154 \pm 31$	$-32 \pm 71$	$-0.97 \pm 0.18$	OB III
IRS 7SE2 .....	4.95	3.06	3.89	13.7	$42 \pm 28$	$-71 \pm 28$	$-85 \pm 100$	$-0.93 \pm 0.34$	WC
	5.08	-4.86	1.47	16.3	$107 \pm 29$	$-19 \pm 29$	$88 \pm 71$	$-0.12 \pm 0.26$	OB III
	5.80	3.20	-4.84	12.6	$-84 \pm 28$	$-134 \pm 27$	$3 \pm 70$	$-0.91 \pm 0.18$	E?
	6.26	1.54	-6.07	15.8	$42 \pm 29$	$102 \pm 29$	$128 \pm 50$	$0.60 \pm 0.27$	OB III?
	6.38	6.33	0.81	14.9	$-163 \pm 29$	$44 \pm 28$	$208 \pm 54$	$0.38 \pm 0.17$	OB III?
	7.11	6.96	1.43	15.5	$-104 \pm 30$	$-42 \pm 30$	$-12 \pm 71$	$-0.18 \pm 0.27$	OB III
	7.45	-4.07	-6.24	15.3	$31 \pm 30$	$91 \pm 33$	$83 \pm 50$	$-0.25 \pm 0.32$	OB III?
	7.87	-7.76	1.36	10.6	$162 \pm 53$	$152 \pm 49$	$148 \pm 50$	$-0.80 \pm 0.22$	OB III?
	8.19	-4.81	6.63	15.8	$54 \pm 32$	$28 \pm 33$	$229 \pm 51$	$-0.99 \pm 0.53$	OB III
	9.73	-6.32	-7.39	12.6	$52 \pm 39$	$-95 \pm 37$	$108 \pm 51$	$0.93 \pm 0.35$	OB III?

confirmed and extended these findings. Adding proper motions to the radial velocities allowed a more constrained analysis (Genzel et al. 2000, 2003; Levin & Beloborodov 2003). In the end, Genzel et al. (2003) considered 26 stars with three-dimensional velocity. They used  $j$ , the normalized angular momentum with respect to the line of sight, to demonstrate the existence of two coherent star systems (Appendix B, eq. [B1]) on near-tangential orbits in projection ( $|j| \simeq 1$ ), one rotating clockwise ( $j \simeq +1$ ) and the other counterclockwise ( $j \simeq -1$ ). Using a  $\chi^2$  argument proposed by Levin & Beloborodov (2003; see also eq. [B2]), they show that both systems fit disk solutions. A total of 12–14 stars form the clockwise system. It is rather thin, and its midplane has an inclination of  $i = 120^\circ \pm 7^\circ$  with respect to the plane of the sky and a half-line of ascending

(=receding) nodes at  $\Omega = 120^\circ \pm 15^\circ$  east of north (the actual numbers quoted in Genzel et al. [2003] are different because of different conventions; a detailed definition of those used in the present paper is given in Appendix A). The corresponding normal vector is  $\mathbf{n} = (n_x, n_y, n_z) = (-0.43, -0.75, +0.50) \pm (0.23, 0.17, 0.11)$ . This system is the one found earlier by Levin & Beloborodov (2003). The second, counterclockwise system in Genzel et al. (2003) is new, counts 10–12 stars, is thicker, and has  $i = 40^\circ \pm 15^\circ$  and  $\Omega = 160^\circ \pm 15^\circ$  [ $\mathbf{n} = (-0.6, -0.22, -0.77) \pm (0.25, 0.23, 0.17)$ ]. The two systems are at large angles relative to each other ( $87^\circ \pm 36^\circ$ ). Tanner et al. (2006), adding seven radial velocities and improving on others, also fit disk solutions on their data (10 stars in the clockwise system, five in the counterclockwise). They find disk solutions in good

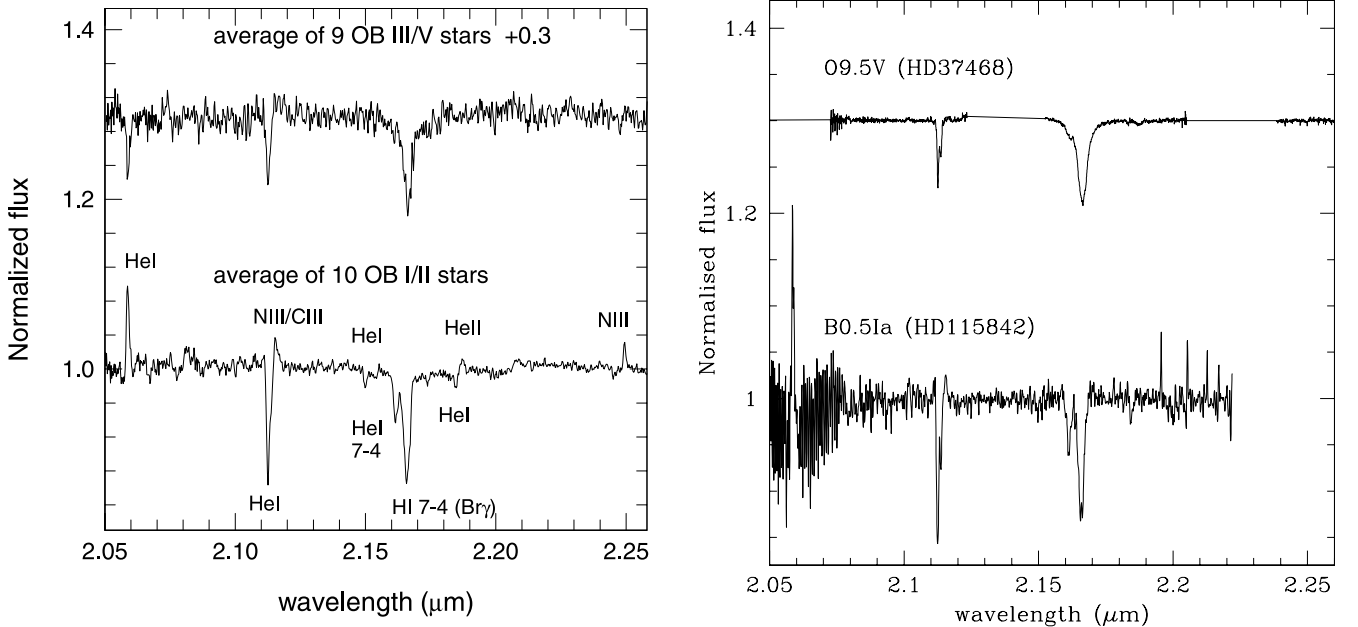


FIG. 2.—*Left*: Co-added, normalized, and baseline-subtracted spectra of the 10 best OB Iab–II supergiants (*bottom*) and the nine best O III–V (*top*) stars in our sample. For each star we determined the velocity and then shifted all stars to a common rest frame. The various transitions are labeled. For the top spectrum a constant of 0.18 was added. *Right*: Templates from Hanson et al. (2005) are overplotted on our spectra. [See the electronic edition of the *Journal* for a color version of the left panel of this figure.]

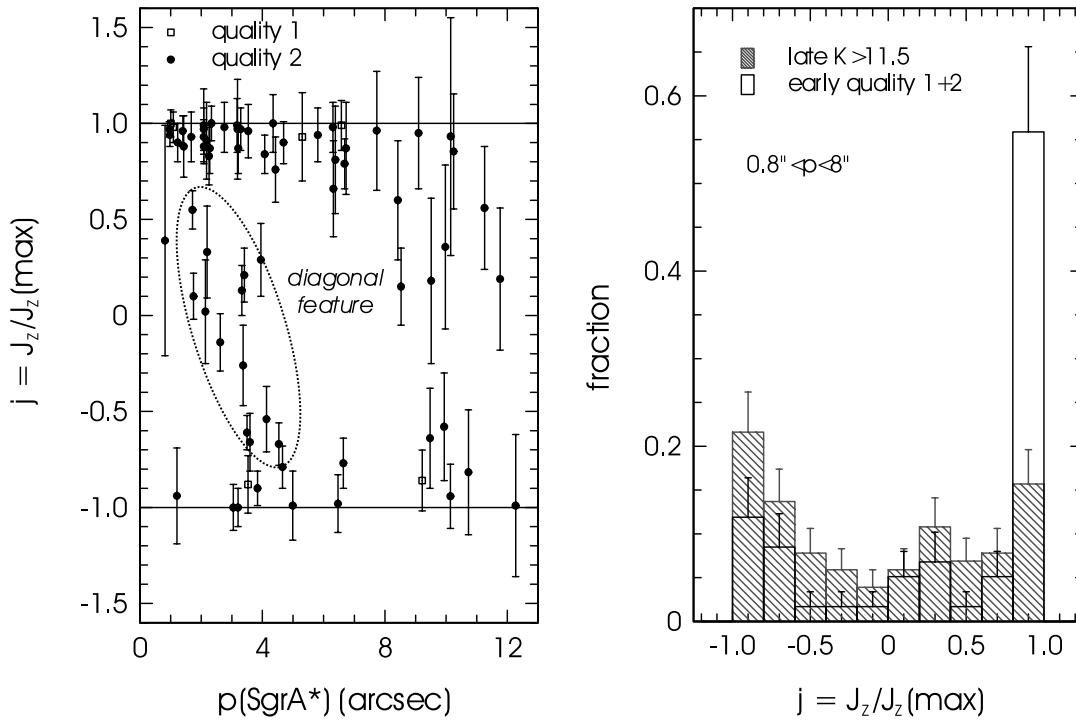


FIG. 3.—*Left*: Distribution of projected and normalized angular momentum on the sky  $j = J_z/J_{z, \max}$  (eq. [B1]) for the early-type stars as a function of projected separation  $p$  from Sgr\* (for  $p > 0''.8$ ). In this diagram stars on projected tangential, clockwise orbits are at  $j \simeq +1$ , while stars on tangential, counterclockwise orbits are at  $j \simeq -1$ . Stars at  $j \simeq 0$  are on projected radial orbits. Filled circles denote the highest quality (2) spectroscopic stars, and open squares denote moderate-quality (1) stars. A DF is apparent on this diagram. It seems statistically significant, but we have no physical unique interpretation to suggest. *Right*: Histogram of the  $j$  distribution of the quality 1–2 spectroscopic stars integrated over  $0''.8 < p < 8''$  ( $N = 59$ ), compared to a sample of  $N = 102 m_K > 11.5$  spectroscopic late-type stars that should be close(r) to relaxation. [See the electronic edition of the Journal for a color version of this figure.]

agreement with their predecessors:  $\mathbf{n} = (-0.42, -0.65, +0.76) \pm (0.05, 0.03, 0.06)$  and  $(-0.23, -0.08, -0.97) \pm 0.13$  (after normalization). From the rather high reduced  $\chi^2$  they get, they conclude that the disks must be somewhat thicker than previously thought, although they make no quantitative statement.

Our new data increase the number of stars and the quality of the velocity measurements very substantially. In Figure 3 we plot the same  $j$  versus  $p$  (the projected distance from Sgr A\*) diagram as in Genzel et al. (2003), adding our new stars. We exclude stars in the central “S” cluster ( $p \leq 0''.8$ ) that appear to be on randomly oriented, elliptical orbits (Ghez et al. 2005; Eisenhauer et al. 2005). For  $p \geq 8''$  the velocities are smaller and proper-motion uncertainties increase. As a result, the typical uncertainty in  $j$  increases to  $\pm 0.3$ – $0.5$  and a detailed analysis is not possible. For this reason we consider in the right panel of Figure 3 the histogram of  $j$ -values for the 59 quality 1+2 stars for the range  $0''.8 \leq p \leq 8''$ . We compare the distribution for the early-type stars to the distribution of 102 late-type stars with  $m_K > 11.5$  in the same range, which serve as a template for a relaxed distribution. A total of 81% of the early-type stars move on near-tangential orbits ( $|j| > 0.6$ ). This is to be compared to 59% for the late-type stars. Early-type stars clearly are preferentially on tangential orbits.

The clockwise system (CWS) at  $j \simeq +1$  is particularly striking and now contains 36 (40) quality 1+2 stars with  $|j| \geq 0.6$  and  $p \leq 8''$  ( $14''$ ). The counterclockwise system (CCWS) is less well populated with 12 (17) stars with the same quality criteria and limits as above. In fact, compared to the late-type distribution in the right panel of Figure 3, the enhancement in counterclockwise stars at  $|j| \geq 0.6$  would not appear statistically significant. We show below, however, that the counterclockwise stars do indeed lie in a common plane, just as the clockwise stars and in contrast to the late-type stars selected with the same criteria. There are

$\simeq 10$  stars at  $p < 8''$  with small projected angular momentum. Of these, several have large error bars in  $j$  and could still be part of the two tangential systems. However, it is interesting to note that these  $\simeq 10$  stars with  $0''.8 < p < 8''$  and  $|j| < 0.6$  lie with a fairly small scatter around a diagonal line that runs from  $(p = 0'', j = 0.6)$  to  $(p = 6'', j = 0)$ . Therefore, this group of stars seems to have some statistical significance, although its physical meaning is not yet clear. We later refer to these stars as the diagonal feature (DF) stars, as they share other noteworthy characteristics.

The  $\chi^2$  approach used by Levin & Beloborodov (2003) and Genzel et al. (2003) has the drawback that it is somewhat indirect. In the following we use a different way of looking for disk structures in our stellar data. This new method is easy to visualize and can demonstrate the existence of a disk independently from the determination of its parameters. We show in Appendix B (eq. [B6]) that, in the plane spanned by  $\varphi$  and  $\cot \theta$  ( $\varphi$  and  $\theta$  being the spherical coordinates of the velocity vectors), stars located in a planar structure must exhibit a telltale cosine pattern. Figure 4 shows the results if stars are coarsely separated into CWS, CCWS, and DF stars. Beside the value of  $j$  ( $j < 0$  for CCWS,  $j > 0$  for CWS, and  $|j| < 0.6$  for DF stars), the only criteria we used were the quality of the data for selection (or rejection), as determined from the average significance of the three space velocities  $(\sum_{k=x,y,z} v_k/\sigma_{vk})/3$  and the significance in the determination of sign  $j$  ( $j/\sigma_j$ ), and the projected distance  $p$  from Sgr A\*. As velocities decrease with  $p$  and proper-motion uncertainties increase with  $p$ , the quality of the velocity and  $j$  determinations decreases with  $p$ . We find that quality 2 stars with velocity and  $j$  significances  $> 3.5 \sigma$  give by far the best determination of  $\varphi$  and  $\theta$ . This essentially selects stars at  $|j| > 0.6$  and  $p < 7''$  into the two tangential systems. The DF is defined only by  $|j| < 0.6$  and  $p < 8''$ . In addition, we also considered more

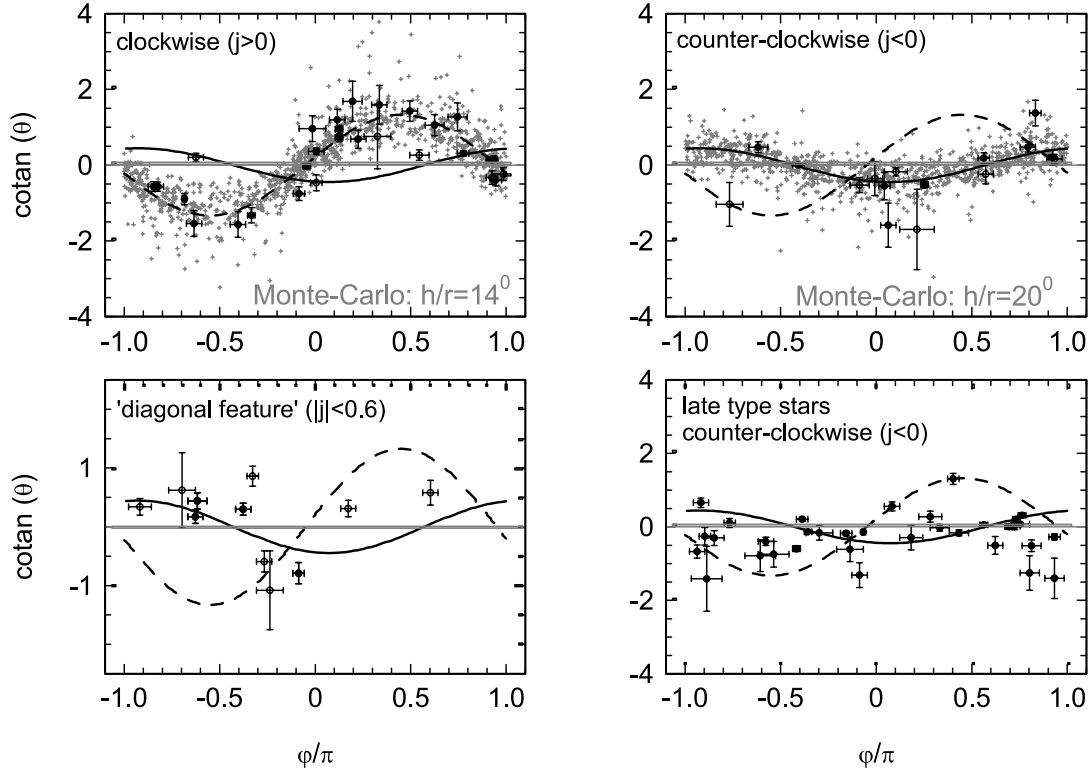


FIG. 4.—Location of various stellar populations in the  $\varphi$ - $\cot\theta$  plane described in § 3.2.1 and Appendix B (eq. [B6]). *Top left*: Clockwise early-type stars ( $j > 0$ ). *Top right*: Counterclockwise early-type stars ( $j < 0$ ). *Bottom left*: DF stars (see Fig. 3:  $|j| < 0.6, p < 8''$ ). *Bottom right*: Counterclockwise late-type stars. Filled circles are quality 2 stars with  $>3.5\sigma$  (average) detections of the three space velocities and (except for the DF stars) determination of  $j$ . Open circles are stars that have somewhat relaxed significance criteria ( $2\sigma$ ). The thick dashed line is the best-fitting clockwise disk ( $i = 124^\circ, \Omega = 99^\circ$ ), and the thick solid line is the best-fitting counterclockwise disk ( $i = 24^\circ, \Omega = 167^\circ$ ). The small plus signs denote Monte Carlo simulations ( $\approx 10^3$  stars) of two disks with these parameters and a Gaussian distribution of opening angles ( $\sigma = 14^\circ$  and  $20^\circ$ , respectively). [See the electronic edition of the *Journal* for a color version of this figure.]

relaxed selection criteria ( $\geq 2\sigma$ ). Our main finding is that there definitely are two well-defined planar structures, at large angles with respect to each other ( $115^\circ \pm 7^\circ$ ), in the early-type star data. One at  $i = 127^\circ \pm 2^\circ$  ( $1\sigma$ ),  $\Omega = 99^\circ \pm 2^\circ$  [ $\mathbf{n} = (-0.12, -0.79, 0.60) \pm 0.03$ ] fits all of the clockwise stars with our quality criteria but one, which is indeed a DF star (Fig. 3). Again, this is the clockwise disk already found by Levin & Beloborodov (2003).

The second structure at  $i = 24^\circ \pm 4^\circ$ ,  $\Omega = 167^\circ \pm 7^\circ$  [ $\mathbf{n} = (-0.40, -0.09, -0.91) \pm (0.07, 0.06, 0.03)$ ] fits all of the counterclockwise stars (a few appear as outliers, but they have large error bars). This second plane is coincident with the second plane identified by Genzel et al. (2003). Remarkably, it also fits very

well 8 of the 11 DF stars. Four of the DF stars are compatible with both disks, one fits the CWS much better, and one (IRS 16SSW) appears to fit neither. Several of the five DF stars that fit best the CCWS have  $j > 0$  and therefore seem to counterrotate in the disk in which they fit best, but  $j < 0$  is not excluded by more than  $\approx 1.5\sigma$ .

Most of the bright stars in the so-called IRS 16 complex a few arcseconds east and southeast of Sgr A\* are part of the CWS. This includes IRS 16C and IRS 16SW. Several stars in the IRS 13E complex, as well as IRS 16NE and IRS 16NW, are part of the CCWS. In Table 4 we list the various planar structures in the GC, including the clockwise and counterclockwise systems. Figure 5 illustrates the relative orientation of these planes. Although

TABLE 4  
PLANAR STRUCTURES IN THE GALACTIC CENTER

Name	$\Omega$	$i$	$n_x$	$n_y$	$n_z$	References
CWS.....	$99 \pm 2$	$127 \pm 2$	$-0.12 \pm 0.03$	$-0.79 \pm 0.03$	$+0.60 \pm 0.03$	
CCWS.....	$167 \pm 7$	$24 \pm 4$	$-0.40 \pm 0.07$	$-0.09 \pm 0.06$	$-0.91 \pm 0.03$	
Galaxy.....	$31.4 \pm 0.1$	$90 \pm 0$	$+0.85 \pm 1E-3$	$-0.52 \pm 1E-3$	$+0.00 \pm 0.00$	1
Northern arm <sup>a</sup> .....	$15 \pm 15$	$50 \pm 30$	$+0.74 \pm 0.34$	$-0.20 \pm 0.28$	$-0.64 \pm 0.40$	2
Bar <sup>b</sup> .....	115	76	-0.41	-0.88	-0.24	3
CND.....	25	70	+0.85	-0.40	-0.34	4

NOTES.—The parameters listed here are defined in Appendix A. They give the orientation of the given disks as two angles, and as one normal vector. Values from other papers have been translated into our conventions.

<sup>a</sup> Northern arm of the minispiral; values are approximate averages for the best defined part (index < 30) in Fig. 6 of Paumard et al. (2004b).

<sup>b</sup> Bar of minispiral.

REFERENCES.—(1) Reid & Brunthaler 2004; (2) Paumard et al. 2004b; (3) Liszt 2003; (4) Jackson et al. 1993.

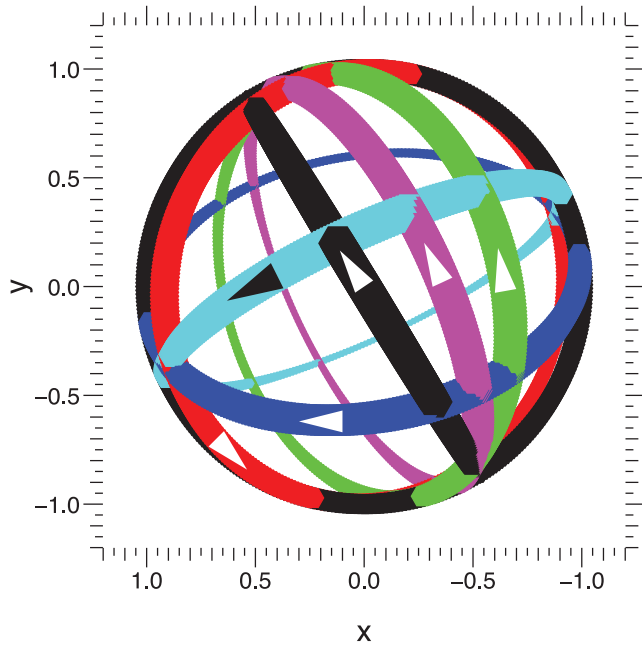


Fig. 5.—Various planar structures in the GC (Table 4): the Galaxy and sky (black), the clockwise (blue) and counterclockwise (red) stellar systems, the northern arm (green) and bar (cyan) components of the ionized minispiral, and the CNM of molecular gas (magenta). Each plane is represented by one ring. The thickness of the ring figures the proximity to the observer. Arrows indicate the direction of rotation.

the CNM and the northern arm of Sgr A West are at relatively low inclination to the plane of the Galaxy, it is clear that the two stellar disks, the bar of Sgr A West, and the Galactic plane are all quite different from each other.

Basically the same results are obtained from the alternative and independent method of Levin & Beloborodov (2003; see also eq. [B2]). For the CWS this method gives  $i = 124^\circ \pm 2^\circ$  and  $\Omega = 100^\circ \pm 3^\circ$ , and for the CCWS  $i = 30^\circ \pm 4^\circ$  and  $\Omega = 167^\circ \pm 9^\circ$ .

Beloborodov et al. (2006) make a detailed analysis of the innermost region of the CWS ( $p < 5''$ ) using the “orbital roulette” method (Beloborodov & Levin 2004), which allows them to derive an independent estimate of the mass of Sgr A\*. This part of the CWS appears quite thin:  $10^\circ \pm 4^\circ$ . The best-fit plane is then  $\mathbf{n} = (-0.14, -0.86, +0.50)$ . In Table 2 we list the  $z$  coordinate they derive for this solution.

### 3.2.2. The Disks Have Moderate Geometric Thickness

The best-fit  $\chi_r^2$  values range between 2.3 and 3.1 for both disk systems, and for equations (B6) and (B2). The disks are very well defined, but the data require a finite thickness. If lower quality stars are added for the fitting, the resulting  $\chi_r^2$  increases to values above 4. We interpret this effect as likely being caused by additional systematic uncertainties in velocity determinations, especially for stars at  $p > 6''$  and for stars with poorer or broader spectral features.

We have carried out Monte Carlo simulations to determine the geometric thickness of the disks. We computed the location of  $\simeq 10^3$  stars each in the  $\varphi$ - $\cot \theta$  plane, assuming a normal distribution for the orbital inclinations to the system’s midplanes. We have varied the  $\sigma_i$  width of these distributions and also taken into account the errors in the velocity determinations. We then compared the resulting model disks with the data to determine the best-fit distributions (Fig. 4). For the clockwise set the best-fitting value is  $\sigma_i = 14^\circ \pm 4^\circ$  ( $\langle |h|/R \rangle = 0.12 \pm 0.03$ ). For the best 11 coun-

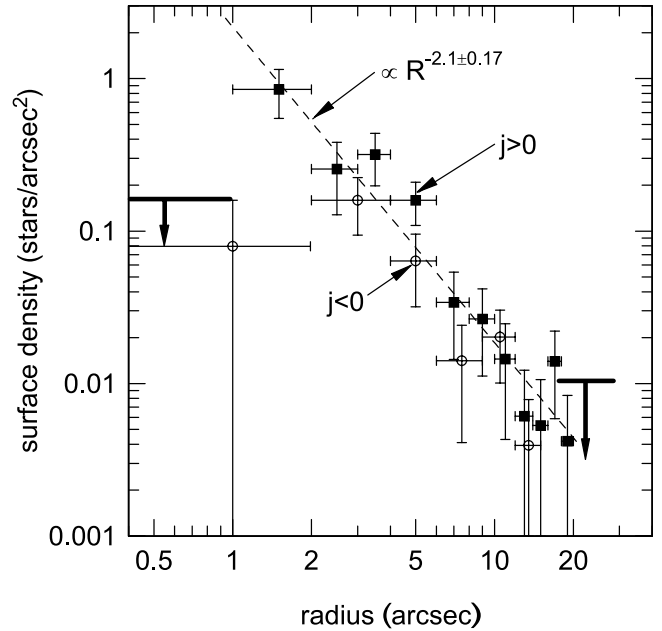


Fig. 6.—Surface density of stars in the clockwise (filled squares) and counterclockwise (open circles) disk systems, as a function of three-dimensional radius from Sgr A\* and derived in the framework of a “thin-disk” model. The surface density distribution of the clockwise stars can be well fitted by an extended disk with a sharp inner edge at  $R \simeq 1''$  and a surface density decreasing outward proportional to  $R^{-2}$ . The CCWS more resembles a ring at  $R \simeq 4''$  (or has a large inner edge of about  $2''$ ) but with the same outward surface density falloff as the CWS. No OB stars are seen outside about  $p \simeq 13''$  (Fig. 1) despite the deep continuous coverage in the northern strip and deep fields. [See the electronic edition of the Journal for a color version of this figure.]

terclockwise stars, the best-fit thickness is  $19^\circ \pm 10^\circ$  ( $\langle |h|/R \rangle = 0.16 \pm 0.06$ ). The two stellar disks have significant but moderate geometric thickness.

### 3.2.3. Steep Radial Density Profile and Inner Cutoff

We have estimated the three-dimensional position of each star by assuming that it is on the corresponding system’s midplane or, in other words, under a very thin disk model assumption. The thickness of the disk introduces an error. The projected position on the CWS midplane of a CWS star at the average elevation is offset by  $\simeq 0.1R$  perpendicular to the line of node ( $0.07R$  for the CCWS). This effect can be in either direction, however, depending on whether the star is in front of or behind the midplane. Therefore, on average, this effect does not introduce a significant bias.

We have then calculated the surface density distribution as a function of true radius for stars with quality 2 and with  $v$  and  $j$  significance  $> 1.5 \sigma$  in the CWS and CCWS. Figure 6 shows the results. The clockwise disk has a well-defined power-law, surface density distribution with an index equal to or approximately  $-2$ . There is a very well delineated inner cutoff, at  $p \simeq R \simeq 1''$ . It is striking that this inner cutoff appears to coincide almost exactly with the outer radius of the central S cluster of randomly oriented B stars (Eisenhauer et al. 2005). The CCWS has a larger inner cutoff ( $\geq 2''$ ) such that it appears to be more like a ring centered at  $R \simeq 4''$ , but this inner radius comes down to roughly the same as that of the CWS when including the DF stars ( $0.8 < p < 8''$  and  $|j| < 0.6$ ). Outside of this inner edge, however, its surface density distribution is very much the same as that of the clockwise system. The larger number of stars of the CWS as compared to the CCWS (excluding DF, factor  $\simeq 2.5$ ) thus is mostly the result of the former extending much farther inward than the latter.

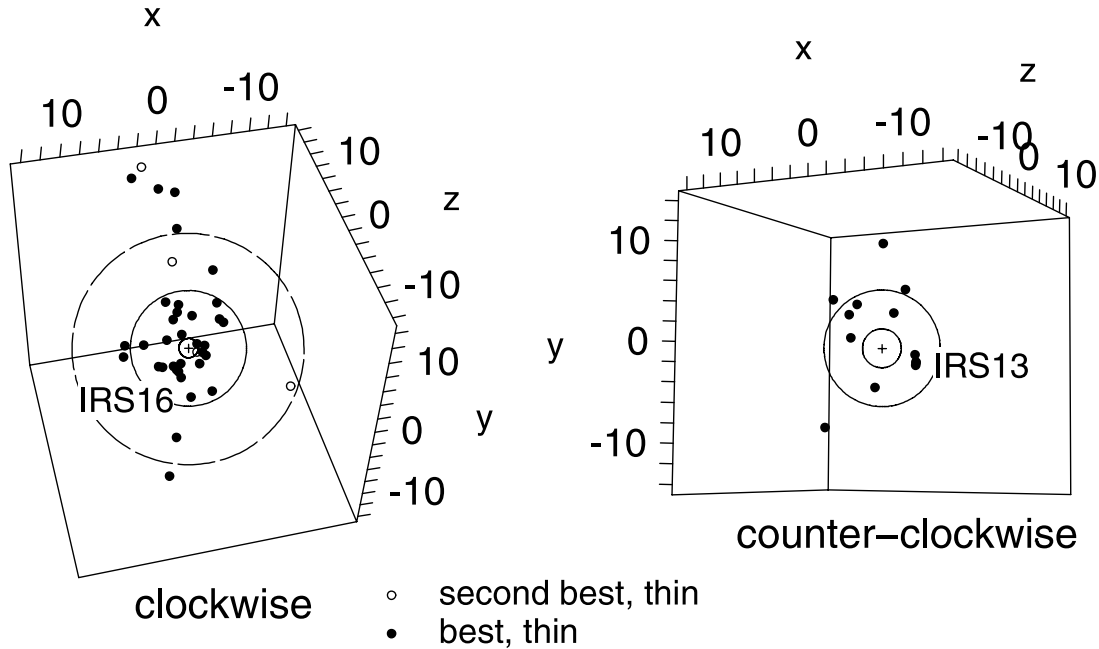


FIG. 7.—Azimuthal distribution of the stars in the clockwise ( $j > 0$ ; left) and the counterclockwise ( $j < 0$ ; right) systems. Filled circles denote the positions of the best stars ( $>1.5 \sigma$  significance of  $z$  determination) in the thin-disk model. Open circles denote the second best stars. The innermost circles denote the inner edges ( $1''$  for the CWS,  $2''$  for the CCWS). The outer filled circles have a radius of  $6''$ , and the outermost, dashed circle (left panel) has a radius of  $12''$ . [See the electronic edition of the Journal for a color version of this figure.]

In addition to this, Figure 1 shows already very clearly that the early-type stars all reside in the central  $p \approx 13''$  ( $\approx 0.5$  pc) region, despite our searches over a much larger region and in several directions. This nondetection of OB stars is a quite robust result. In particular, in the strip stretching from  $y \approx 7''$  to  $24''$  directly north of Sgr A\*, the effective magnitude limit (for significant detection of spectroscopic features in early-type stars) in this field is  $\approx 15.5$  across the entire field ( $\approx 110$  arcsec<sup>2</sup>) and  $>17$  in two deep subsections of about 20 arcsec<sup>2</sup> (H. Maness et al. 2006, in preparation; Fig. 1). This region is close to the visible AO reference star so that the achieved Strehl ratio was high throughout the observations. Judging from the extinction map of Scoville et al. (2003), the excess  $K$  extinction due to local dust is  $<1$  mag throughout this region. This puts a  $1 \sigma$  upper limit of  $\approx 10^{-2}$  per arcsec<sup>2</sup> for O and early B stars outside the cutoff radius of  $p \approx 13''$ . Over the  $>200$  arcsec<sup>2</sup> region outside  $p \approx 13''$  covered by the shallower (spectroscopic  $K$  limiting magnitude  $\approx 13$ ) but wider large-scale mosaics, a similar limit is deduced. This upper limit is consistent with, and strengthens, the  $R^{-2}$  density profile extrapolated to  $p > 13''$ .

### 3.2.4. Isotropic Azimuthal Structure

Figure 7 shows the azimuthal distribution of the stars in the CWS and CCWS when viewed from the pole of the two systems under the model assumption of very thin disks. Again, the radial distribution discussed in the last section, including the  $\approx 1''$  sharp inner edge of the CWS and the tendency of stars in the CCWS to be at large radii, perhaps in a ringlike shape, is apparent. The graphs also clearly show that the azimuthal stellar distribution is azimuthally symmetric to within the still fairly limited statistics of the data. Apparent local “concentrations” exist, but because of small numbers, they are all consistent with statistical fluctuations.

This conclusion is somewhat in contrast to the work of Lu et al. (2005), who have argued that the concentration of five stars near IRS 16SW ( $\approx 1''.5$  east,  $1''.5$  south of Sgr A\*) may be the surviving core of a compact cluster. Their main argument is that the

local two-dimensional velocity dispersion is at a global minimum on this group. While a group of four to six stars corresponding to this “IRS 16 comoving group” is clearly visible in the left panel of Figure 7, to the left and down from center, there are similar such groupings elsewhere in the disk, of similar (low) statistical significance. However, what makes IRS 16 different from other locations in the field is the presence of a “hole” in the CCWS at the same projected location (this hole also has very low statistical significance). Therefore, Lu et al. (2005) probably happen to be measuring the true velocity dispersion within the CWS at the location of IRS 16, whereas elsewhere, their measurement must include stars from the CCWS and therefore naturally be higher.

Another interesting grouping of about three to five early-type stars in a region of less than  $1''$  is IRS 13E,  $\approx 4''$  southwest of Sgr A\*, in the CCWS. This group has attracted recent interest, owing to the proposal by Maillard et al. (2004) that it may be stabilized against tidal disruption by an IMBH. We return to this region in § 3.3.

### 3.2.5. Circular and Noncircular Motions in the Disks

In this section we estimate the eccentricities of the stellar orbits in each disk. This eccentricity is straightforward to derive once the line-of-sight position ( $z$ ) of a star is known (assuming that the potential well and the distance to the GC,  $R_0$ , are known). We have used Monte Carlo simulations to derive estimates of the eccentricity  $e$  of each star, under the assumption that it belongs to one of the two disks. The method we used is described and discussed (including its limitations) in Appendix C. We produced artificial data sets under various assumptions to validate the method. The individual estimates we derive are listed in Table 2, and their histograms for the CWS and CCWS are shown in Figure 8. The completely independent method used by Beloborodov et al. (2006) also allows them to derive stellar eccentricities. The two methods agree well on the individual values.

These histograms show that the distributions of eccentricities of the two systems are quite different. The CWS is made of stars

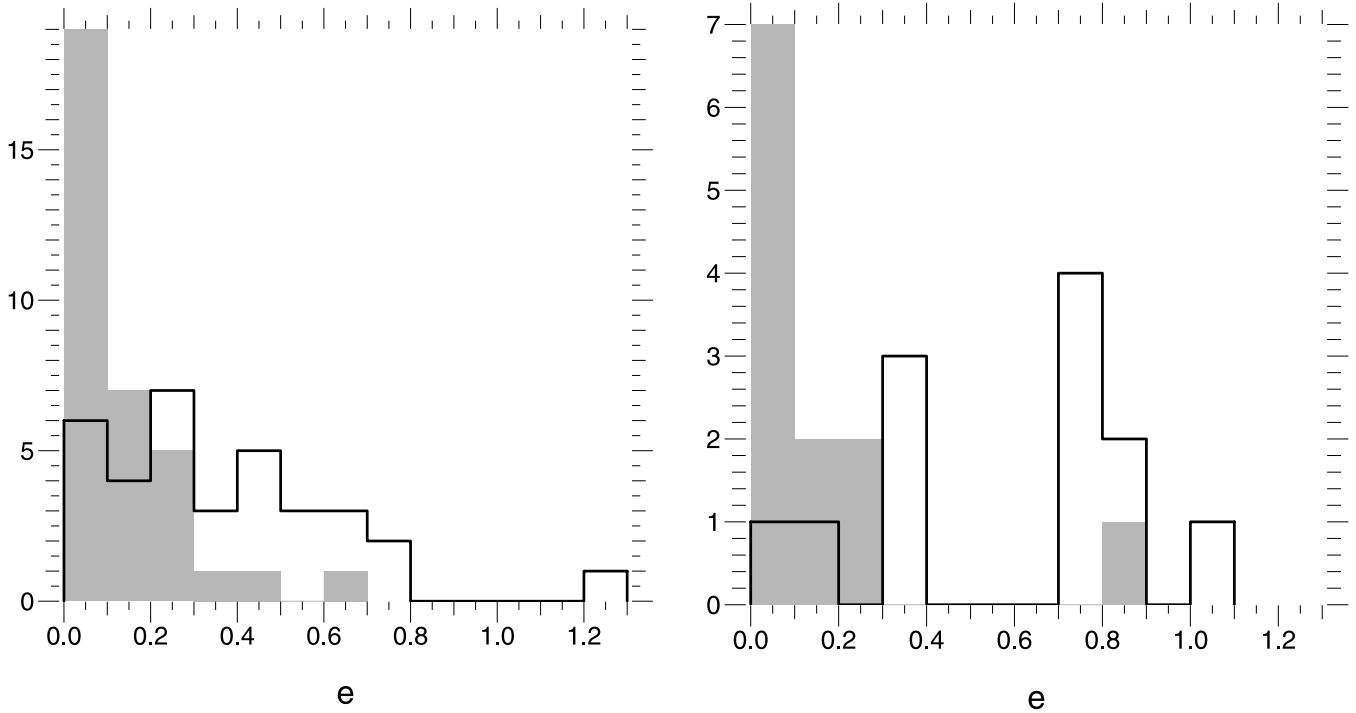


FIG. 8.—Eccentricity distributions in the CWS (*left*) and CCWS (*right*) disks, for both the real data sets (*open histogram*; all stars with  $v$  and  $j$  significance  $> 2\sigma$ ) and artificial data sets for which all stars are assumed to be on circular orbits (*shaded histogram*).

on low to medium eccentricities ( $\lesssim 0.5$ ). For this system, we find only slightly higher eccentricities than what we would derive for a system with the same geometry, on which all of the stars would be on circular orbits. The distribution peaks around  $e = 0.2$ , which is expected given the thickness of the disk ( $\tan 14^\circ \simeq 0.25$ ). The CWS is essentially in low eccentricity, close to circular motion.

On the other hand, the CCWS contains a few low-eccentricity stars, including a peak around  $e = \tan 19^\circ \simeq 0.35$ , but is dominated by a high-eccentricity ( $e \simeq 0.8$ ) population. Three of these stars belong to the IRS 13E complex (§ 3.3), but even when counting these three stars as a single dynamical entity, the conclusion remains that the CCWS is essentially in noncircular motion. The same work performed for the DF stars shows that if these stars live on either of the disks, then most of their eccentricities have to be quite high (very close to 1). These high-eccentricity stars are definitely bound to Sgr A\*.

### 3.3. IRS 13E: A Dissolving Star Cluster and/or the Site of an Intermediate-Mass Black Hole?

The compact, bright source IRS 13E,  $3''$  west and  $1''.5$  south of Sgr A\*, merits special discussion. IRS 13E has several properties that tend to make it unique in the central cluster:

1. It is associated with a bright peak of dust and ionized gas emission in the minispiral, at the edge of the so-called “minicavity” (e.g., Clenet et al. 2004; Paumard et al. 2004b).
2. It harbors at least three bright stars within a radius of  $0''.25$  (Paumard et al. 2001).
3. It is associated with a pointlike X-ray source (Baganoff et al. 2003; Munro et al. 2005).
4. It is associated with a compact centimeter radio source (Zhao & Goss 1998).
5. It is dynamically coherent in that its bright early-type stars participate in a similar three-dimensional space motion (Maillard et al. 2004; Schödel et al. 2005).

Maillard et al. (2004) concluded that IRS 13E consists of at least seven stars, out of which four have highly correlated sky velocities. From the radial velocity difference between two of the sources, they inferred an enclosed mass in excess of  $10^3 M_\odot$  to bind the cluster. They argued that such a mass could not be accounted for by (lower mass) stars in the cluster and that the cluster might contain an IMBH and be the remaining core of an inspiraling star cluster disrupted in the central parsec and stabilized by this IMBH. On the basis of somewhat higher resolution images and more accurate proper motions, Schödel et al. (2005), using four sources, concluded that IRS 13E could be either a local concentration of stars in the counterclockwise disk or a dissolving cluster core. By setting a lower limit to the mass of a stabilizing IMBH of  $10^4 M_\odot$ , they felt that the presence of such an object is quite unlikely for two reasons. First, such a massive BH is not easy to form as a result of core collapse even in a very massive ( $10^6 M_\odot$ ) inspiraling cluster, as core collapse typically creates a central concentration no more massive than  $\simeq 10^{-3}$  of the original cluster mass (Portegies Zwart & McMillan 2002). Second, an IMBH with a mass in excess of  $10^4 M_\odot$  would be inconsistent with the  $2 \text{ km s}^{-1}$  proper-motion velocity limit perpendicular to the Galactic plane deduced by the Very Long Baseline Array observations of Reid & Brunthaler (2004).

#### 3.3.1. IRS 13E Is Not a Background Fluctuation

In the following we first use a statistical approach to determine through stellar counts whether the IRS 13E group can be a chance association of stars in projection. Figure 9 shows a very deep  $H$ -band image we have constructed from a combination of four high-quality NACO images in 2003 (March and May) and 2004 (June and September). Each of these images was individually “cleaned” from the “dirty” AO PSF with the Lucy-Richardson algorithm and then reconvolved with a  $40 \text{ mas}$  FWHM Gaussian. For this purpose we constructed a template PSF from isolated bright stars across the  $\simeq 3''.5$  field. The co-added image was then

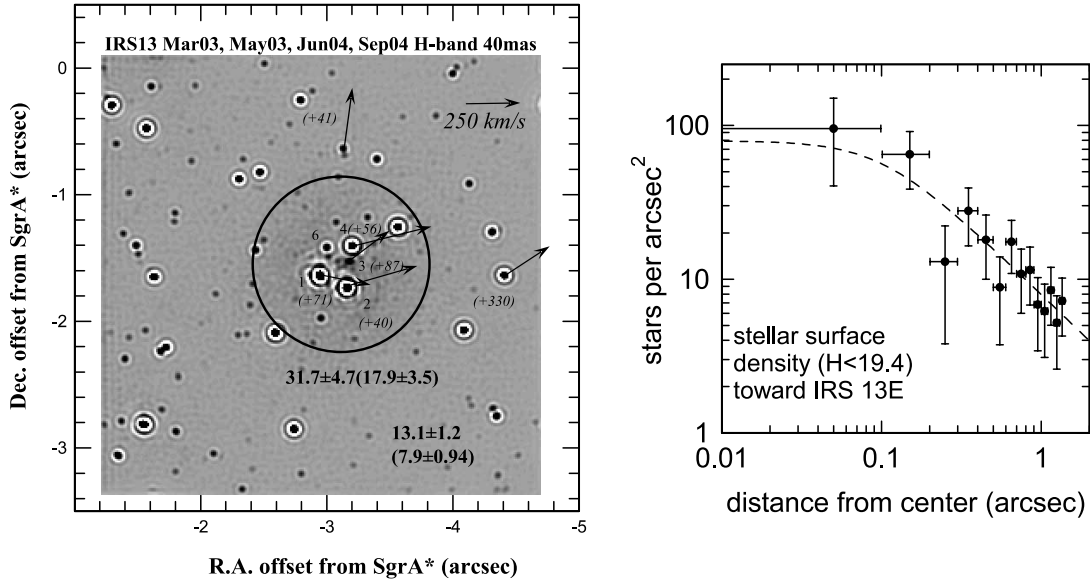


FIG. 9.—*Left*: Sensitive  $H$ -band image of the IRS 13E cluster region constructed from a combination of four NACO  $H$ -band data sets. The brightest stars have  $m_K \simeq 10.7$  and the image has a dynamical range of  $\simeq 9$  mag. The central circle centered on IRS 13E has a radius of  $0''.68$ . The main members of the IRS 13 group are labeled 1–6 (nomenclature of Maillard et al. 2004), with radial velocities given in parentheses. Two other members of the CCWS are in the image and are also marked by their radial velocities. Arrows indicate direction and magnitude of proper motion (calibration in the upper right corner). The numbers next to the circle are the surface densities of stars detected within it with the STARFINDER (Diolaiti et al. 2000) algorithm to  $m_H = 20.4$  and (in parentheses)  $m_H = 19.4$  ( $m_K \simeq 18.5$  and  $17.5$ ), along with their  $1\sigma$  uncertainties. For comparison, we list the surface densities (and uncertainties) to the same limits for the rest of the image shown. *Right*: Surface density of stars to  $m_H = 19.4$ , as a function of separation from the center of IRS 13E at  $x = -3.12$ ,  $y = -1.57$ . The dashed line is fitted to a cluster with density profile  $\propto 1/(r^2 + r_{\text{core}}^2)$  and core radius  $r_{\text{core}} = 0''.17$ . [See the electronic edition of the Journal for a color version of this figure.]

again deconvolved with a Wiener filter with a PSF constructed from fainter isolated stars immediately around IRS 13E. The final image shown in Figure 9 has a dynamical range of 9 mag, and the faintest significant stars have equivalent  $K$  magnitudes of  $\simeq 19.5$ . We then used STARFINDER (Diolaiti et al. 2000) to find and determine the photometry of all stars in the field. We computed the surface densities for a circular aperture of radius  $0''.68$  centered on and encompassing the core of IRS 13E, as well as for the rest of the  $3''.2 \times 3''.2$  region shown in the figure. Figure 9 lists the surface densities (and their  $1\sigma$  uncertainties) to an  $H$  magnitude limit of  $20.4$  ( $m_K \simeq 18.5$ ). In parentheses we also give the same results for the more conservative limit of  $m_H \simeq 19.4$ . The stellar surface density in the central aperture ( $31.7 \pm 4.7$  [ $17.9 \pm 3.5$ ] stars  $\text{arcsec}^{-2}$ ) is 2.3 times greater than in the surrounding region ( $13.1 \pm 1.2$  [ $7.9 \pm 0.94$ ] stars  $\text{arcsec}^{-2}$ ).

Evaluating the significance of this result requires the careful use of Poisson statistics given our prior knowledge. This computation is done in Appendix D. We come to the conclusion that IRS 13E is very unlikely a background fluctuation (a quite conservative upper limit on the likelihood that this is the case is 0.2%). We thus concur with Maillard et al. (2004) that IRS 13E is very probably a local overdensity of stars in the CCWS. We further note that the surface densities given above for the center of IRS 13E are higher than anywhere but in the central cusp within  $0''.7$  of Sgr A\* (Fig. 7 of Schödel et al. 2006). There, the surface density to  $m_H = 19.4$  is  $32.3 \pm 4.7$  stars  $\text{arcsec}^{-2}$ , 1.8 times the value toward IRS 13E. Because of the crowding, it is not possible to estimate an  $m_H < 20.4$  surface density toward Sgr A\*. Toward the center of the IRS 16 region, for instance, the surface densities to  $m_H = 20.4$  ( $19.4$ ) are  $11.4 \pm 1.3$  ( $9.3 \pm 1.2$ ) stars  $\text{arcsec}^{-2}$ , rather similar to the average background density surrounding IRS 13E.

### 3.3.2. The IRS 13E Cluster Is on an Eccentric Orbit

We now return to the remarkable deviation from circular motion of IRS 13E as estimated from the Monte Carlo simulations

in § 3.2.5. In the context of the cluster scenario it is now possible to average the space motions of the four bright stars of IRS 13E and obtain a more precise estimate for the motion of the cluster:  $(x, y) = (-3''.12 \pm 0''.10, -1''.57 \pm 0''.12)$ ,  $(v_x, v_y, v_z) = (-253 \pm 62, 57 \pm 48, 98 \pm 21)$   $\text{km s}^{-1}$ . We have also some more information on the line-of-sight position of the cluster. First, three of the four bright stars in IRS 13E (13E2, 13E3, and 13E4) are formally in the CCWS. 13E1 is formally a DF star and is also compatible with the CCWS (at high eccentricity, however). In the framework of this disk, IRS 13E is at  $z \simeq 1''.5$ . Second, Paumard et al. (2004b) argue that IRS 13E is physically close to the bar component of the ionized minispiral, which they demonstrate is somewhat behind Sgr A\*. Furthermore, Liszt (2003) proposes a model of the bar as a ring orbiting Sgr A\* at  $0.3\text{--}0.8$  pc ( $7''.7\text{--}20''$ ), which would put IRS 13E at  $z = 6''.8\text{--}20''$ . It seems therefore rather safe to assume that IRS 13E is at positive  $z$ . A distance of  $z \simeq 7''$  would be in reasonable agreement with both constraints (proximity to the bar and to the CCWS), with an orbital inclination to the CCWS midplane  $i_{\text{CCW}} \simeq 1.8\text{--}4.2$  ( $1\sigma$ ) times the CCWS half-opening angle. The same Monte Carlo approach as in § 3.2.5 allows us to estimate the eccentricity of the orbital motion of the cluster around Sgr A\* as a function of  $z$  (Fig. 10). Since we have just shown that IRS 13E lies on the right-hand side of this diagram, we can conclude that it is on a fairly eccentric orbit, with  $e \gtrsim 0.5$ .

### 3.3.3. Does IRS 13E Contain an IMBH?

We now ask the question of whether this cluster can be stable without an IMBH at its core. The two elements to check are the tidal forces from Sgr A\* and the internal velocity dispersion. The distribution of stellar surface density as a function of distance from the center of IRS 13E reveals a very small effective core radius (at which the surface density has fallen to half its central value),  $r_{\text{core}} \simeq 0''.17$  (0.0066 pc or 1400 AU; Fig. 9). After subtraction of the background, we count 12 stars to  $m_H = 19.4$

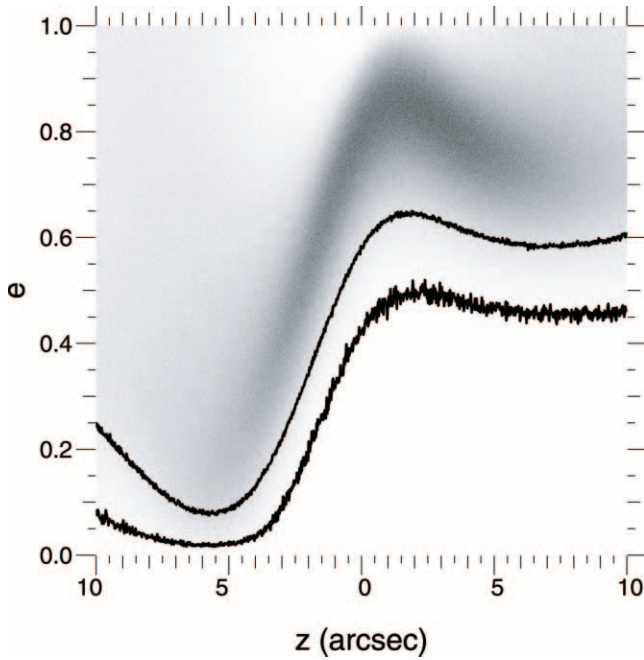


FIG. 10.—Monte Carlo simulation of the eccentricity of the IRS 13E group motion. Given the known distribution of probability for the accessible parameters ( $R_0$ ,  $M_{\text{Sgr A}^*}$ ,  $x$ ,  $y$ ,  $v_x$ ,  $v_y$ ,  $v_z$ ), we have computed the distribution of probability for  $e$  as a function of  $z$  (shading). The two lines trace the 2 and 3  $\sigma$  lower limits on  $e$ . The map is not corrected for the low number depletion issue (Appendix C). The data would be compatible with circular motion if  $z \simeq -5''$ . [See the electronic edition of the *Journal* for a color version of this figure.]

within  $\simeq 0''.35$  ( $\simeq 2$  core radii). For the very simplified assumption that these stars sample the mass function to  $\simeq 5.5 M_\odot$  (zero-age main sequence [ZAMS] for  $m_H \simeq 19.4$  at  $A_K \simeq 3.2$ ) and adopting a flat mass function with  $dN \simeq m^{-1.35} dm$  (§ 3.5), the inferred stellar mass within that radius is about  $350 \pm 100 M_\odot$ . For such a flat mass function the difference between that mass and the mass extrapolated to  $1 M_\odot$  amounts to about  $30 M_\odot$  only. On the other hand, stellar crowding is an issue. Our star counts are unlikely to be complete in the very center of IRS 13E and in the vicinity of its brightest stars. Thus, our mass estimate is obviously a lower limit to the total stellar mass associated with the cluster, and the derived core radius is probably an upper limit. The core density of IRS 13E ( $> 3 \times 10^8 M_\odot \text{pc}^{-3}$ ) is higher than in any other known cluster, except the cusp around Sgr A\*.

IRS 13E is currently at  $\geq 4''$  from Sgr A\*. At this distance, the tidal (“Hill”) radius for such a mass is

$$r_{\text{Hill, IRS 13E}} = \left( \frac{M_*}{M_{\text{BH}}} \right)^{1/3} R = 0''.13 M_{*400}^{1/3}, \quad (1)$$

where  $M_*$  is the mass of the star cluster,  $M_{\text{BH}}$  is the mass of Sgr A\*, and  $M_{*400} = M_*/400 M_\odot$ . The Hill radius is in remarkably close agreement with the observed core radius. However, the distance to take into account is not the current one, but the periapsis distance. This parameter is poorly constrained from our Monte Carlo simulations. It appears that if the cluster were on the CCWS midplane, then the periapsis would be fairly small and the required cluster mass high ( $\geq 10^4 M_\odot$ ). On the other hand, requiring IRS 13E to be (currently) close to the bar as discussed above allows the periapsis distance to be easily above  $4''$ . In this case, the inferred stellar concentration toward IRS 13E may thus be stable against tidal forces, or at least relatively long lived, without the need for an IMBH.

It is interesting to note that, with the same constraints on the current line-of-sight position as above, we can estimate the date of the last periapsis passage of IRS 13E to be  $\simeq 400$ – $1000$  yr ago. It is therefore possible that the past event of active galactic nucleus activity of Sgr A\* 300–400 yr ago (Revnivtsev et al. 2004) was linked with the passage of IRS 13E at its periapsis.

The main argument in Maillard et al. (2004) and Schödel et al. (2005) in favor of high cluster masses ( $10^3$  and  $10^4 M_\odot$ , respectively) came from the velocity dispersion inside the cluster. We still have three-dimensional velocities only for four “stars” in the cluster, one of which, IRS 13E3, is not even a single object but the red core of the cluster, resolved as two sources (3A and 3B) in Maillard et al. (2004), and which we see as no less than seven sources in the present work. This source should therefore be discarded from velocity dispersion analyses, and we remain with only three stars. Our study shows that even though IRS 13E constitutes an overdensity in the central parsec, more than one star out of three in the aperture does belong to the background population rather than to the compact cluster. For this reason, any measurement of the velocity dispersion should be considered with caution. In particular, IRS 13E1, which drives the high value found by Schödel et al. (2005), is formally a DF star rather than a CCWS star and has (when studied independently) a higher eccentricity than the other 13E stars. It is possible that this star is not bound to the cluster. We thus take the conservative position that the evidence for a central dark mass in IRS 13E from the proper-motion data currently is not strong.

### 3.3.4. Formation Scenario

Although the IRS 13E overdensity and the ringlike structure of the CCWS centered on the radius of IRS 13E may appear to favor a dissolving cluster scenario, it is also compatible with the idea of a star cluster formation in situ, within an accretion disk or dispersion ring. If IRS 13E has grown from gravitational instability in the original counterclockwise gas disk, the maximum “isolation mass” that could have collapsed to the present cluster is approximately the mass contained within the annulus of radial thickness  $2r_{\text{Hill}}$ ,

$$M_{\text{isolation}} = A M_{\text{disk}}^{3/2} M_{\text{BH}}^{-1/2} \quad (2)$$

where  $A$  is between 4 and  $\simeq 30$  (Lissauer 1987; Milosavljevic & Loeb 2004). Taking a disk mass of  $5000 M_\odot$  (§ 3.5) and  $M_{\text{BH}} = 4 \times 10^6 M_\odot$ , this isolation mass is at least  $700 M_\odot$ . Our estimated stellar mass thus is also consistent with the concept of local cluster formation within the counterclockwise disk, in agreement with the proposal by Milosavljevic & Loeb (2004).

Overall, it appears that the various pieces of evidence argue for a cluster mass of order  $10^3 M_\odot$ , and that this mass can consist in stars, without a BH. There is some indication, but no firm evidence, of a higher mass. In particular, if IRS 13E is a concentration in the CCWS, we would expect it to be close to the CCWS midplane. This would require a mass  $\geq 10^4 M_\odot$ . Further progress will require more proper motions and radial velocities for the individual faint stars in the cluster.

### 3.4. Stellar Content: The Disks Are Coeval and $\simeq 6$ Myr Old

W-R stars of different subtypes appear at different ages. The number ratios of these subtypes in a coeval population of stars thus give information on the properties of the star-forming event leading to the observed population, in particular its age (Mas-Hesse & Kunth 1991; Vacca & Conti 1992; Schaerer et al. 1997). The evolution of massive stars and the presence of a W-R phase

TABLE 5  
NUMBERS AND FRACTIONS OF EARLY-TYPE SUBCLASSES IN THE TWO DISKS

TYPE	CLOCKWISE			COUNTERCLOCKWISE		
	Number	Fraction	Uncertainty	Number	Fraction	Uncertainty
OB I/II.....	18	0.36	0.08	3	0.15	0.09
OB III/V.....	13	0.26	0.07	6	0.30	0.12
Ofpe/WNL.....	12	0.24	0.07	5	0.25	0.11
WNE.....	1	0.02	0.02	0	0.00	0.00
WC.....	6	0.12	0.05	6	0.30	0.12
Sum.....	50	...	...	20	...	...

are controlled by stellar winds, which depend on metallicity. In principle, the number ratios of W-R to O stars can thus also trace the metal content. However, the strong effects of rotation on the evolution of massive stars modify the duration of the different phases of massive star evolution, especially for the W-R phases (Meynet & Maeder 2003; Maeder & Meynet 2004). Rotation varies from star to star, and the predicted number ratios are affected by this natural spread.

Tables 5 and 6 list the numbers and relative fractions of the different subtypes of early-type stars in the two stellar disks. Compared to observations in other star-forming regions, the W-R/O star fraction in the GC disks is remarkably high. This is partly a selection effect: our number counts are more complete for the supergiants and WN stars than for the dwarfs and WC and WO stars. To first order, the fraction of different types of post-main-sequence supergiants and W-R stars is strikingly similar in the two disks. The fraction of OB (I–V) stars appears to be somewhat higher in the CWS, which may also have a marginally greater fraction of OB supergiants. The striking resemblance in content of massive stars strongly suggests that the two stellar disks are basically coeval (Genzel et al. 2003).

### 3.4.1. Population Synthesis

From these ratios, we can attempt to estimate the age and star formation history of the two disks. In order to investigate the physical properties of the stellar population more quantitatively, we computed population synthesis models for a determination of the expected number ratios under various conditions (star formation history, metallicity, initial mass function [IMF]). Technical details on the method, based on the synthesis code developed by Schaerer & Vacca (1998), are given in Appendix E.

The constant star formation case can easily be ruled out since none of the predicted number ratios match the data. In particular, we do not detect any O3–6 stars. A burst of star formation is clearly preferred. Figure 11 shows the results for such a scenario and a Salpeter IMF. We see that the data are compatible with an age ranging between 4 and 9 Myr. In fact, most of the ratios point to an age of 7–8 Myr, except WC/WN, which is also compatible

with younger ages ( $\simeq 4$ –5 Myr). All ratios involving O stars are certainly upper limits and as such indicate that the deduced age of 7–8 Myr is an upper limit.

The number ratios presented in Figure 11 are usually higher when  $Z$  is larger. However, in most of these diagrams we see that the age derived from the solar metallicity case is similar to the one derived from the twice solar metallicity case. The only exception is the ratio WC/(W-R+O) for which the  $Z_{\odot}$  model predicts values lower than what we observe. This may be an indication that  $Z$  in the central cluster is slightly supersolar, but given the uncertainty in the current observed number ratios of W-R to O stars, this needs to be confirmed by much more robust analyses.

Choosing a burst of star formation with finite duration has the effect of shifting the timescale by 2 Myr but does not change significantly the shape of the function giving the number ratios as a function of time. We believe that a duration of  $\leq 2$  Myr is quite consistent with our data. Longer bursts would also create large numbers of red supergiants. Only three such supergiants (IRS 7, IRS 19, and IRS 22; Blum et al. 1996) are observed in the central parsec.

As for the IMF, adopting a flatter one increases the strength of the first “bump” around 4 Myr observed in the evolution of the number ratios (Fig. 11) but does not strongly modify the ratios at later epochs. For a top-heavy IMF the number ratios of the CWS are consistent with a burst of star formation  $\simeq 4$  Myr ago (the solution at  $\simeq 6$ –7 Myr being still valid).

### 3.4.2. Hertzsprung-Russell Diagram

We have also modeled the ages of the luminosity class I–V OB stars directly by placing them on an infrared (IR) Hertzsprung-Russell diagram and comparing the data with isochrones. This requires the knowledge of both an absolute luminosity (or magnitude) and effective temperatures for all stars (Appendix F). We restricted ourselves to the OB stars since for the evolved massive stars (Ofpe/WN9 and W-R stars), no calibration of effective temperature as a function of spectral type exists (mainly due to the strong effect of winds on the stellar properties of such objects). We excluded from our analysis those stars for which the spectral classification is uncertain. We also excluded the S stars near the central BH.

The results are shown in Figure 12. Overplotted are Geneva evolutionary tracks taken from the database of Lejeune & Schaerer (2001). Isochrones for 4 and 8 Myr are also shown. We see that most of the stars are located between these two isochrones. In particular, there are no stars on the left side of the bend at  $\log T_{\text{eff}} \simeq 4.5$  in the 4 Myr isochrones, showing that the stellar population is older. There are a few outliers—although with large error bars—cooler than the 8 Myr isochrone, but an older age is not likely in view of the presence of numerous W-R stars not included in this diagram for reasons highlighted above. The present age estimate

TABLE 6  
RATIO OF DIFFERENT SUBTYPES

Type 1/Type 2	Clockwise	Counterclockwise	All
W-R/O.....	0.61	1.22	0.75
W-R/(W-R+O).....	0.38	0.55	0.43
WNL/(W-R+O).....	0.24	0.25	0.24
WNE/(W-R+O).....	0.02	0.00	0.01
WC/(W-R+O).....	0.12	0.30	0.17
WC/WN.....	0.46	1.2	0.67

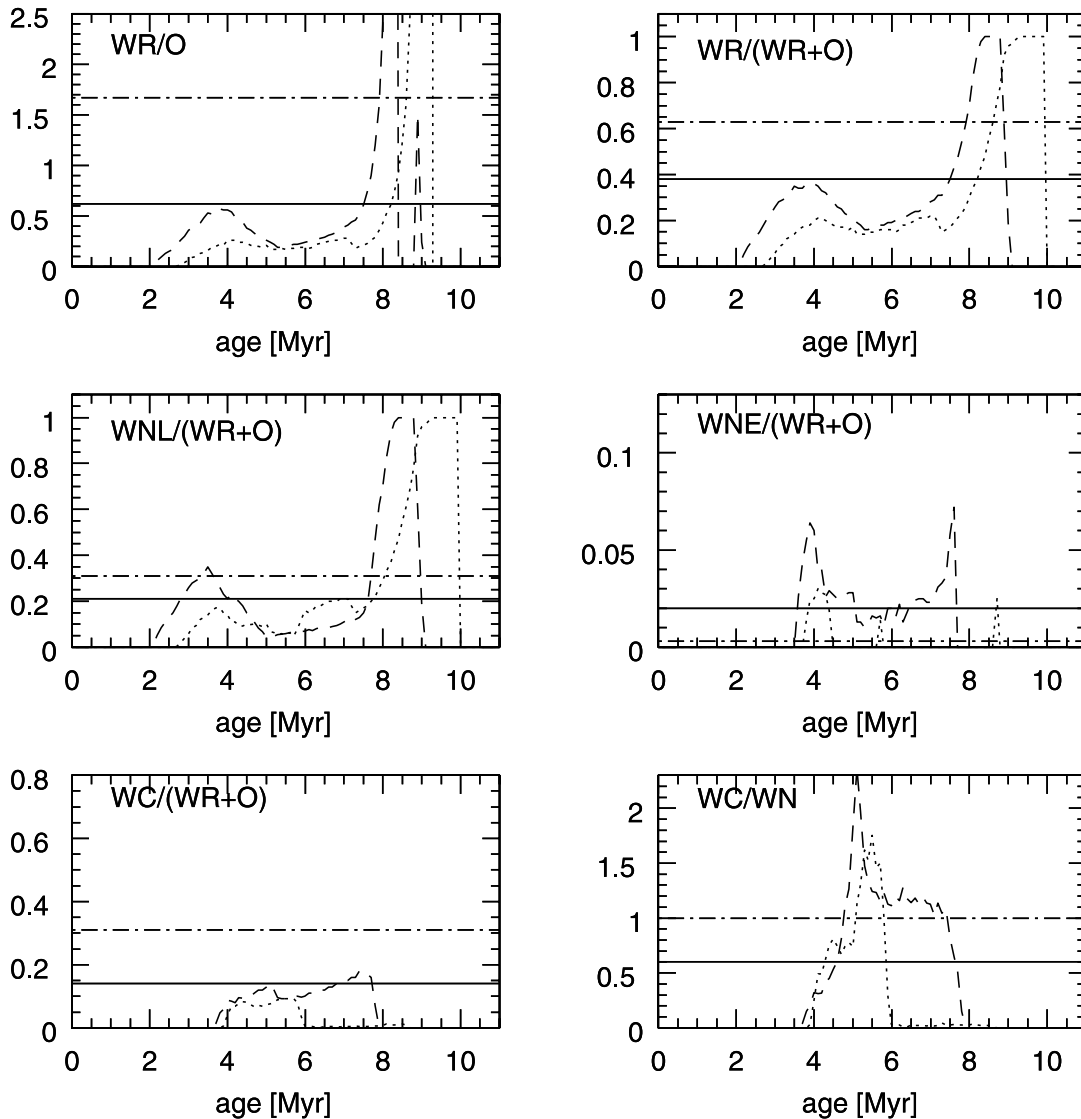


FIG. 11.—Number ratios of different types of massive stars as a function of time under the assumption of a single burst of star formation. The adopted IMF has a slope of 2.35, a lower mass limit of  $1 M_{\odot}$ , and an upper mass limit of  $100 M_{\odot}$ . We have used Geneva evolutionary tracks with rotation for solar (*dotted line*) and twice solar metallicity (*dashed line*). The horizontal solid lines correspond to the observed values and are upper limits. The second peak in the W-R/O ratio is due to massive stars experiencing a blue loop. [See the electronic edition of the *Journal* for a color version of this figure.]

confirms the result of the previous section. The OB population in the GC is 4–8 Myr old. The fairly large age uncertainties are inherent to our methods of assigning  $M_K$  and  $T_{\text{eff}}$  (Appendix F). The fact that two different studies give the same result is rather convincing and reassuring.

In summary, the stellar disks in the GC have formed about  $6 \pm 2$  Myr ago. They are coeval to within about 1 Myr. The burst duration did not exceed about 2 Myr. The present results thus are in excellent agreement with the earlier findings of Tambllyn & Rieke (1993) and Krabbe et al. (1995). Krabbe et al. (1995) invoked a decaying burst of star formation 7 Myr ago to explain the observed stellar population and its ionizing properties.

### 3.5. Flat Mass Function and Total Mass of the Stellar Disks

In this section we use the stellar number counts as a function of  $K$  magnitude to constrain the (initial) mass function of the young stars in the central parsec. In Figure 13 we show two independent methods for estimating the  $K$ -band luminosity function (KLF) of the stars in the disks. Obviously the key issues are the screening against late-type, background interloper stars and

the determination of the number of early-type stars at the fainter levels ( $m_K > 14$ –15) where the spectroscopy is not yet possible or incomplete. Filled circles in Figure 13 denote the KLF constructed from the deep counts from NACO  $H/K_s$ -band data in the IRS 16 region (size  $2''.5 \times 2''.5$ ) and IRS 13E cluster (size  $0''.7$ ; see Fig. 9) and assuming that extinction is constant. We eliminated from those counts 11 stars that are spectroscopic late-type stars but otherwise assume that the non-early-type background toward these regions can be neglected. The steep rise in the counts probably indicates that this assumption is violated at  $m_K > 15$ . Our alternative approach (*filled squares*) was to compute counts for the entire region  $0''.8 \leq p \leq 6''$  and require that the detected stars either are spectroscopic early-type stars or (for the fainter stars) have  $|j| > 0.6$ . This method thus suppresses the background by taking advantage of the tangential motion of most of the early-type stars, in contrast to the late-type stars (Fig. 3). Again, the steep rise of the counts at  $m_K > 15$  probably signifies a dramatic increase in the interloper background contribution. We note that for both methods the average “spectroscopic completeness limit” is 13.5–14. The different slopes of the two observed luminosity

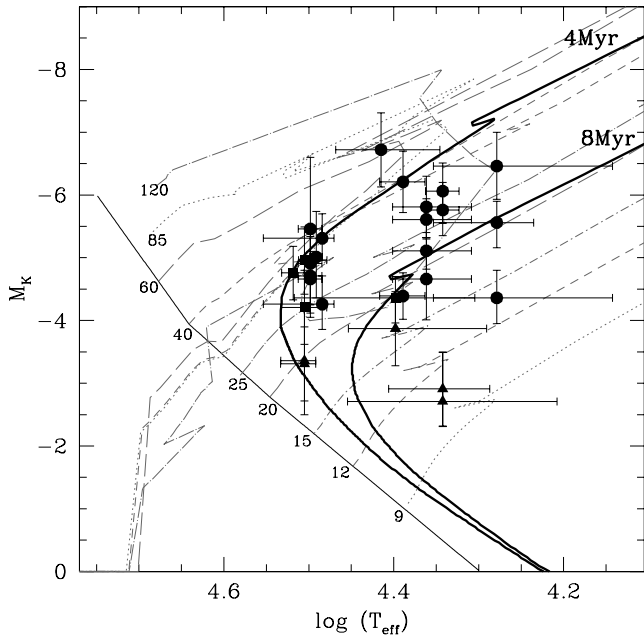


FIG. 12.—Location of the OB supergiants (filled circles), giants (filled squares), and dwarfs (filled triangles) in an IR Hertzsprung-Russell diagram. The numbers indicate the initial mass of the star on the tracks starting from the ZAMS (thin solid line). The two thick solid lines are two isochrones for 4 and 8 Myr. The tracks (various dotted/dashed lines) are based on Geneva models without rotation (Lejeune & Schaerer 2001). [See the electronic edition of the Journal for a color version of this figure.]

functions in the spectroscopically “safe” region at  $m_K < 13$  are possibly a result of a decrease in average stellar luminosity with  $p$ . The two methods more or less span the uncertainty box on the number of faint and bright stars to include in the luminosity function of the young stellar population. For comparison, the thick solid and dashed lines show two model luminosity functions with different mass functions. Both lines are based on the population synthesis code STARS (Sternberg 1998; Sternberg et al. 2003) with solar metallicity Geneva tracks and assume a burst model of age 6 Myr and duration 1 Myr compatible with the results of the last section. The solid line is for a standard  $0.7\text{--}120 M_\odot$  Salpeter IMF ( $dN/dm \simeq m^{-2.35}$ ), while the dashed line is for a much flatter mass function ( $dN/dm \simeq m^{-0.85}$ ). It is obvious that a Salpeter mass function cannot fit the very flat counts toward IRS 16/13E and does only marginally so for  $m_K > 12$ . Both observed luminosity functions show a large excess above the Salpeter model for  $m_K < 11$ . However, this range is dominated by very bright evolved stars that may not be properly accounted for by the Geneva tracks. Putting the largest weight on the more reliable range  $11 < m_K < 14$ , which includes the OB dwarfs and giants, we conclude that the data require a mass function flatter than a Salpeter function by  $\simeq 1\text{--}1.5$  dex.

With this result we can now estimate empirically the total stellar mass in the two stellar disks. As before, we exclude from the following discussion the cluster of B stars in the central cusp around Sgr A\*. There are in total  $\simeq 53$  and 20 observed OB+W-R stars (quality 1+2) in, respectively, the CWS and CCWS. Recent stellar evolution models with rotation by Meynet & Maeder (2003) and Maeder & Meynet (2004) indicate that only stars more massive than  $\simeq 20\text{--}25 M_\odot$  will go through the W-R phase we observe in the GC. Likewise, the faintest OB stars we are able to detect in the GC must have ZAMS masses in excess of about  $20 M_\odot$ . We thus assume that the observed OB and W-R stars represent the (initial) mass range of  $20\text{--}120 M_\odot$ . Adopting an

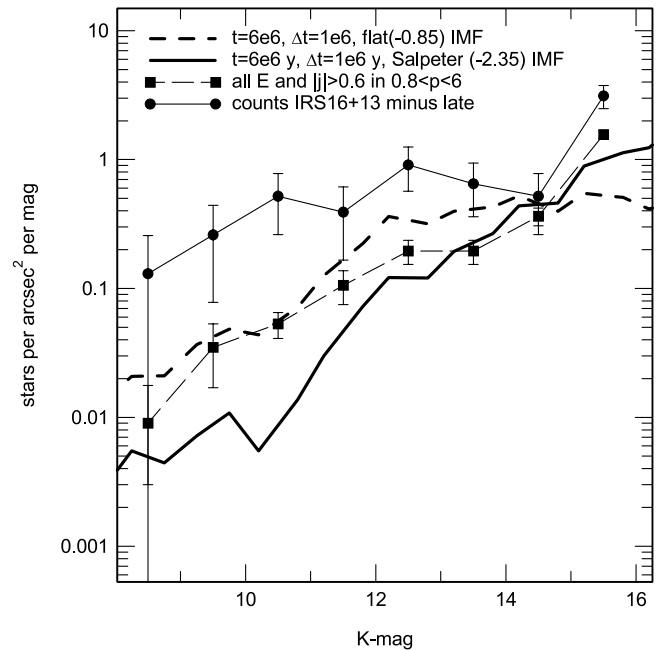


FIG. 13.—KLF. Filled circles and squares denote two ways of estimating the KLF of the early-type stars. The filled circles denote counts from the best high-resolution  $H/K$ -band NACO images in the IRS 16 and IRS 13 regions where spectroscopically identified late-type stars have been eliminated. The filled squares denote all stars with  $|j| > 0.6$  and  $0.8 < p < 6''$  that are not spectroscopically identified as late-type stars in our proper-motion/spectroscopic catalog (T. Ott et al. 2006, in preparation). The thick solid line represents the KLF at age  $t = 6$  Myr of a cluster formed in a burst of duration  $\Delta t = 1$  Myr with Salpeter IMF ( $dN/dm \simeq m^{-2.35}$ ), normalized to the average of the observed counts in the  $m_K = 14\text{--}15$  bin. The long-dashed thick line denotes the KLF of a burst with the same age and duration as above, but with much flatter IMF ( $dN/dm \simeq m^{-0.85}$ ). [See the electronic edition of the Journal for a color version of this figure.]

IMF with a slope of  $\Gamma = -1.35$  and  $-0.85$  ( $dN/dm = m^\Gamma$ ) required to fit the  $K$ -band luminosity function, the total mass in  $\geq 20 M_\odot$  stars is  $2700\text{--}3100 M_\odot$  for the CWS and  $1000\text{--}1200 M_\odot$  for the CCWS (the corresponding numbers for a Salpeter [ $\Gamma = -2.35$ ] mass function would be  $2100$  and  $790 M_\odot$ ). Extrapolating from the number of  $\geq 20 M_\odot$  stars to the entire mass range above  $\simeq 1 M_\odot$  yields a total stellar mass of  $3800\text{--}3500 M_\odot$  for the CWS and  $1420\text{--}1320 M_\odot$  for the CCWS. Given that  $\Gamma > -2$ , these mass estimates are relatively insensitive to the choice of lower mass cutoff and slope. The corresponding numbers for a Salpeter mass function would be  $10^4$  (CWS) and  $3900 M_\odot$  (CCWS). Obviously these estimates are lower limits since we almost certainly have not detected all of the  $M \geq 20 M_\odot$  stars yet. We can establish a rough upper limit to the numbers of missing O stars by counting all stars ( $0.8 < p < 13''$ ) in our proper-motion list (T. Ott et al. 2006, in preparation) that are on near-tangential, clockwise orbits ( $j > 0.6$ ). In Figure 3 we showed that only 24% of late-type stars but 60% of the early-type stars reside in this range. Given that there are approximately the same number of late- and early-type stars ( $\simeq 100$  each) to  $m_K \simeq 13.9$ , equivalent to an O8–9 V dwarf, the above criterion may select a sample with  $\simeq 71\%$  early-type stars. In our proper-motion sample there are 35 such stars that are not spectroscopic early- or late-type stars. Hence, an upper limit to the correction factor for missing early-type stars with  $M \geq 20 M_\odot$  in each system is about  $(53 + 0.71 \times 35)/53 = 1.5$ . We conclude that the total stellar content in the CWS and CCWS is  $\leq 6000$  and  $2200 M_\odot$ , respectively.

These estimates (or limits) are fully consistent with two other and completely independent lines of argumentation. In the first, Nayakshin et al. (2006) consider the precession and warping that

is induced by one of the stellar disks on the other, and vice versa. They study the evolution of the apparent thickness of the disks with time, as a function of their masses. They require the thickness to be as observed (§ 3.2.2) at  $t = 4$  Myr. Depending on whether the original configuration was two thin disks in circular motion, or whether the counterclockwise disk was initially an inspiraling cluster with significant radial motion, Nayakshin et al. (2006) find masses of between 5000 and 15,000  $M_\odot$  for the CWS and between 5000 and 10,000  $M_\odot$  for the CCWS. The 4 Myr age assumed in their work is somewhat smaller than what we deduced in § 3.4. These masses thus are strict upper limits.

Nayakshin & Sunyaev (2005) have pointed out another argument for a flat IMF and for stellar masses  $< 10^4 M_\odot$  owing to the weakness of extended X-ray emission in the central parsec. Nayakshin & Sunyaev (2005) argue that the bright X-ray emission of young T Tauri stars is a handle for probing the low-mass end of the mass function. For a  $< 10$  Myr old stellar component and a Salpeter mass function the predicted diffuse X-ray flux in the central parsec exceeds the observed value of Baganoff et al. (2003) and Muno et al. (2005) by a factor of 20–100.

From these various arguments it is safe to conclude that the mass function of the young stars in the GC is indeed flat and that the total stellar mass contained in the clockwise disk does not exceed  $\simeq 10^4 M_\odot$ . The corresponding limit for the CCWS is probably  $\simeq 5000 M_\odot$ . Our deep observations of the northern field (Table 1 and H. Maness et al. 2006, in preparation) also strongly suggest that there is no “reservoir” of B stars tidally stripped from the inspiraling cluster at larger radii that would point to many missing lower mass stars. We thus believe that the flat mass function we, Nayakshin et al. (2006), and Nayakshin & Sunyaev (2005) deduce approximates an IMF, unaltered by dynamical effects.

## 4. DISCUSSION

### 4.1. Origin of the Stellar Disks

What have we learned from the new observations and their analysis? Let us summarize the key conclusions:

1. The large majority of the early-type stars in the central parsec (excepting those in the central cusp around Sgr A\*) reside in one of two well-defined rotating disks. These disks are oriented at large angles with respect to each other and to the Galactic plane. One rotates clockwise in projection, the other one counterclockwise. The CWS has 2.5 times as many massive stars as the CCWS.

2. The disks have a well-defined inner radius (edge). The more populated clockwise disk has an inner edge at  $p = 1''$ , just outside the central B star cluster in the Sgr A\* cusp. Its azimuthal distribution is isotropic. The inner edge of the counterclockwise disk is farther out. This system thus resembles more a ring.

3. Both disks have an outer density profile scaling as  $\Sigma \simeq R^{-2}$ . No O/W-R stars (in all directions) and lower mass B stars (toward the north) are present outside the central  $p = 13''$  region.

4. The disks have a finite but moderate thickness,  $\sigma_i = 14^\circ \pm 4^\circ$  ( $\langle |h|/R \rangle = 0.12 \pm 0.03$ ) for the CWS and  $19^\circ \pm 10^\circ$  ( $\langle |h|/R \rangle = 0.16 \pm 0.06$ ) for the CCWS.

5. Almost all of the stars in the CWS are on low eccentricity, close to circular orbits.

6. On the contrary, most stars on the CCWS appear to be on eccentric orbits.

7. The IRS 13E group of early-type stars appears to be the center of a larger local concentration of stars with  $\geq 12$  ( $K \leq 17.5$ ) members and total stellar mass of order  $10^3 M_\odot$ . It appears to have a large orbital eccentricity ( $e > 0.5$ ). This concentration represents the second largest stellar density in the central parsec, second only to the central Sgr A\* cusp, and is among the highest

known core densities ( $> 3 \times 10^8 M_\odot \text{pc}^{-3}$ ). It is unlikely to be a projection effect. IRS 13E is compact enough that it may be long lived in the tidal field of the central BH, even without invoking a central IMBH. It may be a slowly dissolving star cluster embedded in the CCWS.

8. The stellar disks are coeval to within 1 Myr, have an age of  $6 \pm 2$  Myr, and must have formed over a time period  $\leq 2$  Myr.

9. The total stellar mass associated with each of the two disks does not exceed  $10^4 M_\odot$ .

10. The (initial) mass function of these disks is flatter than a Salpeter mass function by 1–1.5 dex.

Let us review the two star formation scenarios in view of this “report card,” for each of the two systems.

#### 4.1.1. The In Situ Star Formation Scenario Is in Good Agreement with the Data

The presence of two well-defined kinematical systems seems to require two separate events of star formation. This is actually somewhat problematic whatever the formation scenario is, since these two events must have occurred basically at the same time. However, the two events are allowed to be separated by  $\simeq 1$  Myr from each other. This time span is sufficient for star formation to remove most of the gas from the first disk before the second one starts forming. The minimum time needed to form stars can be estimated as follows. Once the disk becomes gravitationally unstable, instabilities are believed to grow in the disk on a dynamical timescale (e.g., Toomre 1964), i.e.,  $(60 \text{ yr})(R/1'')^{3/2}$ . In addition to that, accretion of gas onto protostars is limited by the Eddington accretion rate onto these, which sets the stellar mass doubling timescale to about 1000 yr (e.g., Nayakshin & Cuadra 2005). Taken together, these two conditions constrain the minimum duration of the star formation episode to about  $10^4$  yr. Therefore, both gaseous disks are not required to have been in the central parsec at the same time. The in situ scenario passes points 1 and 8.

Points 2 and 3 are also reasonably natural in the context of an accretion disk. The minimum radius where the gravitational instability can form stars may be estimated as follows. In order for the disk to be self-gravitating at radius  $R$ , the accretion disk surface density  $\Sigma_{\text{gas}}$  must be larger than a minimum value (e.g., Fig. 2 of Collin & Hure 1999; Levin 2006), which is approximately given by  $\Sigma_{\text{min}} = 10^4 M_4 M_\odot / (\pi R_a^2)$ , where  $M_4$  is the minimum unstable disk mass in units of  $10^4 M_\odot$  (see top panel in Fig. 1 of Nayakshin 2005) and  $R_a$  is the radius  $R$  in arcseconds. At the same time, for a given dimensionless accretion rate  $\dot{m}$ , in units of the Eddington accretion rate, and the disk viscous  $\alpha$ -parameter, the standard accretion disk model (Shakura & Sunyaev 1973) predicts that  $\Sigma_{\text{gas}} = \Sigma_{\text{SS}} \propto R_a^{-3/5}$ . Therefore, stars may be able to form only at disk radii greater than

$$R_{\text{min}} \simeq 0.4 \alpha^{4/7} M_4^{5/7} \dot{m}^{-3/7}. \quad (3)$$

Given the crude nature of these estimates and uncertainties in  $\alpha$  and  $\dot{m}$ , this estimate of  $R_{\text{min}}$  is reasonably close to the observed inner disk cutoff radius (precise values for both  $\alpha$  and  $\dot{m}$  are uncertain but should be reasonably close to unity in the case of a massive self-gravitating disk).

The radial stellar density profile  $\Sigma$  may be expected to follow the initial gas surface density,  $\Sigma_{\text{gas}}$ , if star formation *instantaneously* consumed most of the gas disk. Interestingly, the observed  $\Sigma$  varies as  $R^{-2}$ , as expected in a

$$Q = \frac{c_s \Omega}{\pi G \Sigma} \simeq 1 \quad (4)$$

marginally stable stationary self-gravitating disk (Lin & Pringle 1987; Collin & Hure 1999; Thompson et al. 2005;  $Q$  is the Toomre parameter; Toomre 1964). A time-dependent self-gravitating disk left to its own devices will also develop a steep surface density profile,  $\Sigma_{\text{gas}} \simeq R^{-3/2}$  (Lin & Pringle 1987), again close to the observed steep profile, especially when compared with the standard Shakura & Sunyaev (1973) profile that scales as  $R^{-3/5}$  at large radii (when assuming a constant opacity, e.g., eq. [20] in Svensson & Zdziarski 1994). However, the timescales needed for the disk to go through a significant mass transfer in radial direction are prohibitively long:

$$t_{\text{visc}} \simeq \Omega^{-1} \left( \frac{M_{\text{BH}}}{M_{\text{disk}}} \right)^2 \simeq 3 \times 10^8 \text{ yr} \left( \frac{R}{10''} \right)^{3/2} \left( \frac{M_{\text{disk}}}{10^4 M_{\odot}} \right)^{-2}, \quad (5)$$

where  $\Omega$  is the Keplerian angular frequency.

The thickness (point 4) of the disks is also consistent with the expectations: even though the gas (and stellar) disks should be initially quite thin, they thicken somewhat due to relaxation ( $h/R \simeq 0.1$  after a few times  $10^6$  yr; eq. [15] in Nayakshin & Cuadra 2005) and get warped due to the gravitational torque applied by each disk on the other one (Nayakshin & Cuadra 2005; Nayakshin et al. 2006). The low eccentricities of the orbits in the CWS (point 5) are the natural outcome from a marginally stable disk.

The disk mass necessary for a classical disk to fragment is  $\gtrsim 10^4 M_{\odot}$ , just above the higher limit on the current stellar mass (point 9). This discrepancy is not worrisome. A fraction of the gas in the disks may have been expelled through stellar feedback (either escaping the central region or being redistributed and later accreted by Sgr A\*). In addition, the disk surface density was perhaps not a smooth function of radius. In that case, the instability criterion  $Q = 1$  may have been reached in parts of a less massive disk, which would otherwise have been stable.

Formation of massive stars would not be unexpected in the accretion disk star formation scenario. The initial mass of the disk fragment collapsing to form first gravitational condensations in the disk should be of order  $M_{\text{frag}} = \rho_{\text{disk}} h^3$ , which can be estimated for the marginally self-gravitating disk at  $Q \simeq 1$  to be only  $\simeq 0.01 M_{\odot}$  (e.g., see the bottom left panel of Fig. 3 of Collin & Hure 1999; while their estimate was made for  $M_{\text{BH}} = 10^6 M_{\odot}$ ,  $M_{\text{frag}}$  is a weak function of the supermassive BH mass). Nevertheless, since the requisite gas densities in the accretion disk are several orders of magnitude higher than even those in molecular cores, Bondi-Hoyle and Hill accretion rate estimates yield very high accretion rates onto these fragments,  $\dot{M} > 10^{-3} M_{\odot} \text{ yr}^{-1}$ . With this stars double their mass at the rate limited by the Eddington limit, which is of order 1000 yr (Goodman & Tan 2004; Nayakshin & Cuadra 2005; Fig. 2). Thus, as little as  $10^5$  yr of such accretion would lead to very massive stars. In addition, stellar mergers could contribute to the growth of the massive stars. Finally, the first collapsed object may be more massive than the estimate above if the radiative cooling rate is only marginally sufficiently fast to allow disk gravitational collapse (see, e.g., the second simulation in Gammie 2001), or turbulent “pressure” support is important in preventing smaller clouds to collapse (McKee & Tan 2003). For these reasons, a top-heavy mass function (point 10) may be natural in the context of the in situ scenario. Future detailed work is warranted to delineate the dominant mode of massive star growth in the observed stellar disks.

Therefore, the in situ accretion disk scenario fits perfectly for the CWS. There remain, however, two points to be clarified for the CCWS: the high eccentricity of the orbits (point 6) and the

presence of a very dense star cluster (point 7). At first glance these two points seem to be strong clues in the direction of the infalling star cluster scenario. However, the latter point is resolved if the in situ model is amended with the possibility that gravitational collapse in the disk can lead to local cluster formation. The likely occurrence of this process has already been pointed out by Milosavljevic & Loeb (2004). The large eccentricities in the CCWS are not incompatible either with the accretion disk scenario. It is possible that the progenitor accretion disk did not circularize before forming stars, since the disk fragmentation may have occurred on a short dynamical timescale. Alternatively, gravitational interaction between IRS 13E and the gaseous disk may drive the former’s eccentricity (Goldreich & Sari 2003). Both of these ideas will be investigated in greater detail in the future. Overall, the in situ scenario seems acceptable for the CCWS, with some open theoretical questions.

#### 4.1.2. The Inspiring Cluster Scenario Is Unlikely

The inspiring cluster scenario is also able to fulfill more or less easily most of the points of the report card above. The core density of IRS 13E ( $> 3 \times 10^8 M_{\odot} \text{ pc}^{-3}$ ) is greater than the core density required for a cluster to sink deep into the central parsec before disruption ( $10^7 M_{\odot} \text{ pc}^{-3}$ ). Nevertheless, the inspiring scenario seems to fail on point 3 and fails on point 9 in a way that we deem fatal.

First of all, models of such an infalling cluster show that the cluster should lose a lot of stars during the inspiral, leaving a stellar population with a shallow radial profile extending over several parsecs in the radial direction, in contradiction to point 3. Gürkan & Rasio (2005) argue that this discrepancy can in principle be overcome by initial mass segregation in the cluster. In this way, the stars that are lost at large distance from the center are lower mass stars below our detection limit, and all of the detectable stars are brought in the central parsec. No quantitative analysis has been done so far, however, so that it is not clear whether the mass segregation–evaporation process can bring all of the OB stars into the central 0.5 pc, with a density profile as sharp as the observed one, and not leave a telltale population of B stars at  $R > 0.5$  pc (which we do not observe).

Even if this strong mass segregation were possible, we would be observing all of the  $> 20 M_{\odot}$  stars initially in the cluster. The total initial mass of the cluster could not exceed  $17,000 M_{\odot}$  for the CWS and  $6500 M_{\odot}$  for the CCWS, even assuming a Salpeter IMF. The total mass required to make a cluster inspiral from far out (a few tens of parsecs) into the central region within an O star lifetime is  $> 10^5 M_{\odot}$  (Gerhard 2001; McMillan & Portegies Zwart 2003; Kim et al. 2004; Gürkan & Rasio 2005). The inconsistency between the data and the models is a factor of  $\gtrsim 6$  for the CWS and  $\gtrsim 15$  for the CCWS.

Therefore, taken together, these points favor strongly the in situ accretion disk model for the formation of both stellar disks in the central parsec. We conclude that the clockwise disk almost certainly resulted from in situ star formation in a dense gas disk. The most obvious process starting such a disk is the infall of a large gas cloud (Morris 1993; Genzel et al. 2003), followed by dissipation of its angular momentum through shocks in a “dispersion ring” (Sanders 1998). The in situ star formation scenario is also plausible—and certainly much more plausible than the infalling cluster scenario—for the CCWS assuming that eccentric orbits and cluster formation can be understood within the framework of the model.

We do not have an explanation for the near-simultaneous occurrence of two star formation events 6 Myr ago, followed by little since then, and preceded by little for tens of millions of

years (Blum et al. 2003). It is unavoidable to conclude that the epoch 4–9 Myr ago must have been a very special one for the GC. It is interesting and relevant to note in this context that the other two young, massive star clusters in the central 50 pc, the Arches and Quintuplet clusters, have comparable stellar masses ( $10^4 M_\odot$ ), stellar content (WC/WN, etc.), ages (2–7 Myr), and (flat) mass functions (Figer et al. 1999; Figer 2003; Stolte et al. 2005). We might speculate that star formation across the GC was triggered a few million years ago by a global event, such as an interaction with a passing satellite galaxy that raised the pressure in the central interstellar medium and/or led to increased cloud/cloud collisions.

#### 4.2. Origin of the Central B Star Cluster by Scattering from a Sea of B Stars

We end by briefly commenting on the proposal of Alexander & Livio (2004) that the B stars in the central cusp are the result of the capture of B stars on near-loss cone orbits, originally unbound to the central BH, following a three-body, direct exchange scattering process with the central massive BH and  $\simeq 10 M_\odot$  stellar BHs residing in the central cusp.

This elegant and attractive proposal requires the presence of a “reservoir” of B stars originally at large distances from the central hole. In the specific model presented by Alexander & Livio (2004) the captured fraction of  $\geq 3 M_\odot$  B stars is about  $10^{-4}$  for a constant star formation scenario. With  $\geq 15$  B stars currently observed in the central cusp (Eisenhauer et al. 2005), a total reservoir of about  $1.5 \times 10^5 \geq 3 M_\odot$  B stars (and  $1.5 \times 10^4 \geq 15 M_\odot$  stars) is required for the mechanism to work. The surface density in the reservoir depends on its spatial extent. Alexander & Livio (2004) consider stars originating between 0.5 (where stars are on unbound orbits relative to the massive BH) and 2.5 pc (where the orbits are still marginally Keplerian) and find that the required surface density over that area is about 10 B stars arcsec $^{-2}$ . The deep observations reported toward the northern field (Table 1) limit the number of  $m_K < 16.5$  B stars to about 0.4 stars arcsec $^{-2}$ . The discrepancy is a factor of 25. The current observations appear to exclude the capture of unbound stars by the mechanism proposed by Alexander & Livio (2004). Alternatively the reservoir may be the stellar disks themselves. The exchange capture efficiency of such bound, short-period stars is still under investigation. Due to crowding, it is not yet possible to securely identify B V stars, such as populate the S cluster in the inner arcsecond (Eisenhauer et al. 2005), throughout the disks. While it is possible that some of the stars we identify as OB III/V are B V stars

(Table 5), deeper spectroscopy is required for a full census of the B V content of the disks.

## 5. CONCLUSIONS

We report firm spectroscopic detections of 41 OB stars (luminosity classes I–V) in the central parsec. The new data resolve a decade-old puzzle of the “missing O stars.” Some of these stars seem He- and N-rich (OBN stars).

We confirm the presence and define the properties of the two young star disks first presented by Levin & Beloborodov (2003) and Genzel et al. (2003).

The disks rotate about the center and are at large angles with respect to each other. They have a very well defined inner radius, a radial surface density profile scaling as  $R^{-2}$ , and a moderate geometric thickness. In one of the disks (the clockwise, IRS 16 system) almost all stars are on close to circular orbits. However, in the other, counterclockwise, IRS 13E system, most of the stars (including the IRS 13E cluster) orbit on eccentric orbits. Star counts suggest that IRS 13E is a long-lived cluster of stellar mass  $\geq 400 M_\odot$ . It is the cluster with the highest known core density after the cusp around Sgr A\* itself:  $> 3 \times 10^8 M_\odot \text{pc}^{-3}$ .

The star disks are coeval within  $\simeq 1$  Myr and have formed  $\simeq 6$  Myr ago. The stellar mass function is significantly flatter than Salpeter, setting a limit to the total stellar mass in the disks of about  $1.5 \times 10^4 M_\odot$ .

The constraints just discussed strongly suggest that the stars in the IRS 16 disk were formed in situ from a dense gaseous accretion disk. They were not transported into the central parsec by an inspiraling massive star cluster. On balance the same conclusion seems plausible (but not incontrovertibly proven) for the IRS 13E disk. In that case, the IRS 13E cluster must have formed within the disk.

We are grateful to Margaret Hanson for giving us access to her new atlas of near-IR spectra of OB stars prior to publication. We thank Eliot Quataert, Todd Thompson, and Norman Murray for many useful discussions on star formation in disks. We also thank Daniel Schaerer and William D. Vacca for making their population synthesis code available. T. A. acknowledges support by Minerva grant 8484 and a New Faculty grant by Sir H. Djangoly, CBE, of London, UK. F. M. acknowledges support from the Alexander von Humboldt Foundation. Finally, we would like to thank the anonymous referee for his useful comments.

## APPENDIX A

### CONVENTIONS USED IN THIS PAPER

We use the usual astronomical Cartesian coordinate system, in offsets from Sgr A\*:  $x = \cos \delta d\alpha$  increases eastward,  $y = d\delta$  increases northward, and  $z = dD$  increases forward along the line of sight from the observer. We occasionally use spherical coordinates:

$$\varphi = \arctan\left(\frac{y}{x}\right), \quad \theta = \arccos\left(\frac{z}{\sqrt{x^2 + y^2}}\right), \quad R = \sqrt{x^2 + y^2 + z^2}, \quad (\text{A1})$$

$$x = R \sin \theta \cos \varphi, \quad y = R \sin \theta \sin \varphi, \quad z = R \cos \theta. \quad (\text{A2})$$

When discussing orbital planes, we use the orbital elements defined in Aller et al. (1982, p. 382), adapted for defining an oriented disk, which is consistent with Eisenhauer et al. (2005). The disks are first defined by the orientation of their line of nodes, which is the intersection of the disks (which contain Sgr A\*) with the plane of the sky (also containing Sgr A\*). More precisely, we refer to the ascending (=receding) half of this line. The position angle of the line of nodes  $\Omega$  is the angle between the north direction and this ascending half of the line of nodes, increasing east of north (counterclockwise). The second element necessary to define these oriented

disks is the inclination  $i$ , measured on the ascending half of the line of nodes, from the direction of increasing  $\Omega$  to the direction of motion on the disk:

$$\begin{aligned} 0^\circ \leq i < 90^\circ &\Rightarrow \text{counterclockwise projected rotation,} \\ 90^\circ < i \leq 180^\circ &\Rightarrow \text{clockwise projected rotation.} \end{aligned}$$

An equivalent way to define these disks is to give the three Cartesian coordinates of their normal vector. The rotation of the stars on the disks is then always counterclockwise when visualized from a point toward which the normal vector is pointing. A disk is counterclockwise (in projection) when the  $z$  coordinate of its normal vector is negative and clockwise when it is positive:

$$n_x = \sin i \cos \Omega, \quad n_y = -\sin i \sin \Omega, \quad n_z = -\cos i. \quad (\text{A3})$$

The spherical coordinates of the normal vector relate to  $i$  and  $\Omega$  but are not equal to them:

$$\varphi_{\mathbf{n}} = -\Omega, \quad \theta_{\mathbf{n}} = 180^\circ - i. \quad (\text{A4})$$

## APPENDIX B

### DISCRIMINATING STAR DISKS

Genzel et al. (2003) defined the sky-projected angular momentum (or normalized angular momentum with respect to the line of sight) as

$$j = \frac{J_z}{J_{z,\max}} = \frac{xv_y - yv_x}{(x^2 + y^2)^{1/2} (v_x^2 + v_y^2)^{1/2}}. \quad (\text{B1})$$

It is a simple way to distinguish stars on projected tangential orbits ( $|j| \simeq 1$ ) from stars on projected radial orbits ( $j \simeq 0$ ) and to distinguish stars on projected clockwise orbits ( $j \simeq +1$ ) from stars on projected counterclockwise orbits ( $j \simeq -1$ ). They fit disk solutions to the data by minimizing as a function of the normal vector  $\mathbf{n}$  the following quantity, introduced by Levin & Beloborodov (2003):

$$\chi^2 = \frac{1}{N-1} \sum_{k=1}^N \frac{(\mathbf{n} \cdot \mathbf{v}_k)^2}{(\mathbf{n} \cdot \boldsymbol{\sigma}_k)^2}, \quad (\text{B2})$$

where  $\mathbf{v}_k = (v_{x,k}, v_{y,k}, v_{z,k})$  is the velocity vector and  $\boldsymbol{\sigma}_k = (\sigma_{x,k}, \sigma_{y,k}, \sigma_{z,k})$  is the corresponding velocity uncertainty of the  $i$ th star ( $O_x$  points eastward,  $O_y$  northward, and  $O_z$  away from observer). The unit vector  $\mathbf{n}$  describes the orientation of the normal vector to a common plane in which all  $N$  stars are assumed to move.

There is a more straightforward way to find a disk in the data, which does not rely on fitting. Consider the three-dimensional space velocity of star  $k$  ( $k = 1 \dots N$ ) in spherical coordinates (eq. [A1]),

$$\mathbf{v}_k = (v_{x,k}, v_{y,k}, v_{z,k}) = \|\mathbf{v}_k\| (\sin \theta_k \cos \varphi_k, \sin \theta_k \sin \varphi_k, \cos \theta_k). \quad (\text{B3})$$

Assuming that all  $N$  stars are in the plane of a common disk with normal vector

$$\mathbf{n} = (n_x, n_y, n_z) = (\sin i \cos \Omega, -\sin i \sin \Omega, -\cos i)$$

(see eq. [A3]), then all stellar velocity vectors must obey

$$0 = \mathbf{n} \cdot \mathbf{v}_k = \sin i \cos \Omega \sin \theta_k \cos \varphi_k - \sin i \sin \Omega \sin \theta_k \sin \varphi_k - \cos i \cos \theta_k, \quad (\text{B4})$$

$$\sin i \sin \theta_k \cos(\Omega + \varphi_k) = \cos i \cos \theta_k, \quad (\text{B5})$$

$$\cot \theta_k = \tan i \cos(\Omega + \varphi_k). \quad (\text{B6})$$

In the plane spanned by  $\varphi$  and  $\cot \theta$ , stars located in a planar structure thus must exhibit a telltale cosine pattern.

## APPENDIX C

### THE PROJECTION EFFECTS ON THE DETERMINATION OF THE ECCENTRICITY

For the Monte Carlo simulations in § 3.2.5, for each star we assumed normal distributions for  $v_x, v_y, v_z, R_0$  ( $7.62 \pm 0.32$  kpc; Eisenhauer et al. 2005), and  $M_{\text{Sgr A}^*}$  [ $(3.61 \pm 0.32) \times 10^6 M_\odot$ ; Eisenhauer et al. 2005;  $x$  and  $y$  have been left out as they play a minor role in the error budget]. The potential well is assumed to be dominated by Sgr A\*, which should essentially be true for the region where our measurements are most reliable ( $p < 8''$ ). We have drawn  $z$  as a uniform variable ( $|z| < 20''$ ). For each one of the  $10^6$  realizations (per star), we have computed the eccentricity  $e$  and the inclination to the midplane of the system to which the star belongs ( $i_{\text{CW}}$  and  $i_{\text{CCW}}, i_{\text{CCW}}$  for short). We then constructed the two-dimensional histograms of these two parameters [maps of  $P(i_{\text{CCW}}, e)$ ]. In order to validate our

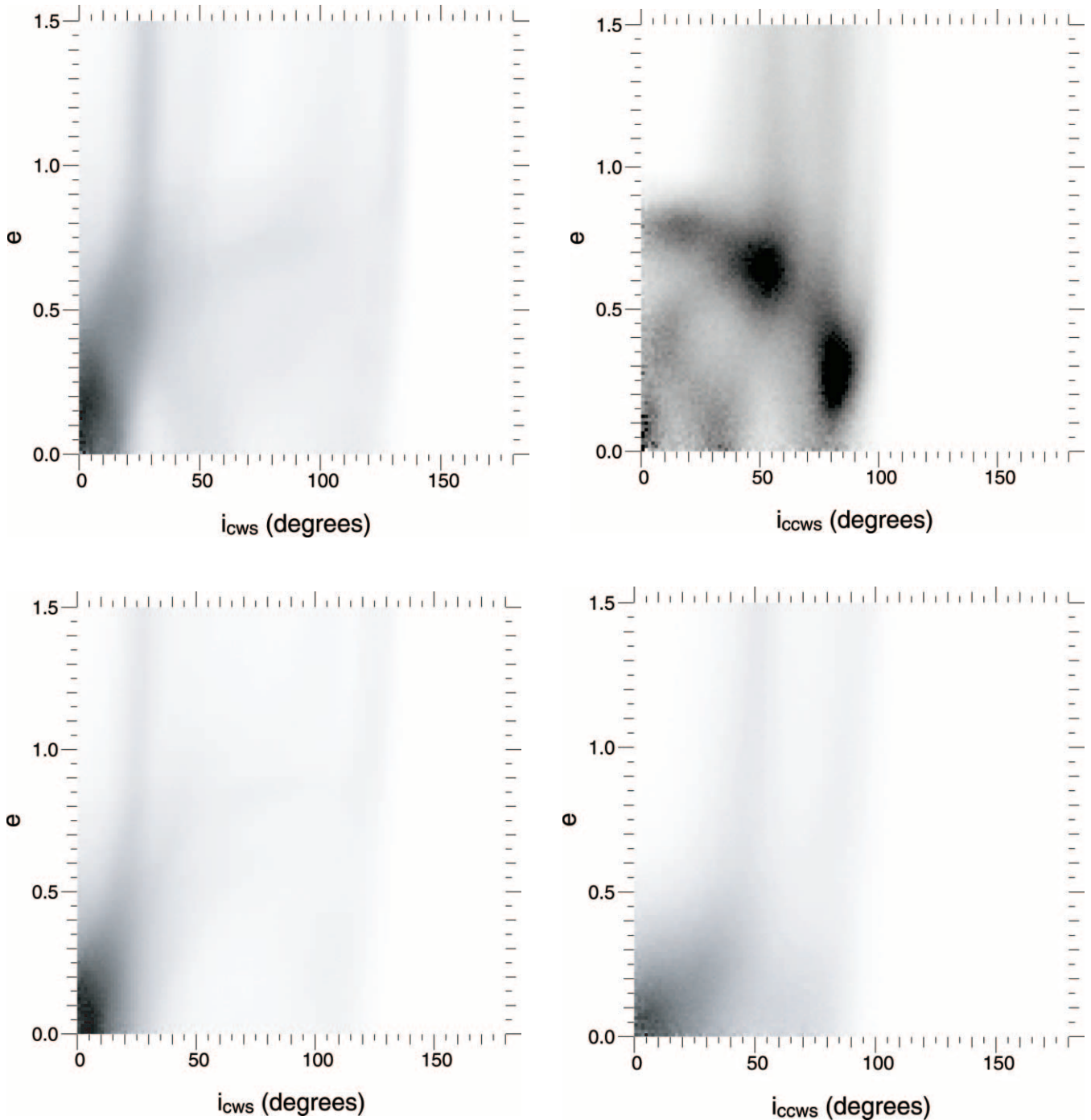


FIG. 14.—Co-added  $e$  vs.  $i_{(C)CWS}$  two-dimensional histograms  $P(i_{(C)CWS}, e)$  ( $z$  uniformly distributed with  $|z| < 20''$ , linear gray scale) for all stars in the following systems: real CWS and CCWS stars (top left and right, respectively;  $p < 8''$ ), and artificial CWS and CCWS stars on circular orbits (bottom left and right, respectively). The real and artificial CWS maps are quite similar, whereas the CCWS ones are very different from each other.

method, we have performed the same analysis on several sets of artificial data that assumed a single eccentricity (including circular case) for all stars and the same geometry as the CWS and CCWS, introducing errors typical of the real systems.  $R_0$  and  $M_{Sgr A^*}$  have been varied to check their influence on the conclusions.

In these two-dimensional histograms, strong depletions were observed close to  $e = 0$  and  $i_{(C)CW} = 0$ . This is simply because of the uncertainties and the functional dependency of  $e$  and  $i_{(C)CW}$  on the three-dimensional velocity (the true errors on  $v_x$ ,  $v_y$ , and  $v_z$  are unlikely to be all smaller than their respective  $1 \sigma$  error bar *at the same time*). We have approximately corrected this effect by dividing the histograms by  $[1 - \exp(-e/0.35)]$  and  $[1 - \exp(-i_{(C)CW}/20^\circ)]$ . This makes the two-dimensional histograms look smooth and the values of  $e$  determined for the artificial stars have the right statistics (peaking close to the assumed eccentricity). The correction affects only small eccentricities in practice ( $e \lesssim 0.2$ ).

Figure 14 shows the sums of the histograms of all stars for each one of the CWS and CCWS, for both the real data and artificial data in which all stars are on circular motion. These co-added  $e$  versus  $i_{(C)CW}$  histograms yield a striking result: whereas the map for the

CWS much resembles the corresponding artificial data set that assumes circular motion, with a maximum toward ( $e = 0, i_{\text{CWS}} = 0^\circ$ ), this is not the case for the CCWS—for this system, the most prominent feature of the map is a (quarter of) ring running from ( $e = 0.8, i_{\text{CCW}} = 0^\circ$ ) to ( $e = 0, i_{\text{CCW}} = 80^\circ$ ). Such a ringlike structure on the two-dimensional histogram of a star is the sign that this star can be either on the disk ( $i_{\text{C}CW} = 0$ ) or on a circular orbit ( $e = 0$ ), but not both at the same time. Since indeed most of the maps of CCWS stars exhibit this ring, and since they cannot all be at high inclination, we can already conclude that CCWS stars have typically high eccentricities.

From these maps, we can go further and estimate the eccentricity for each star. To do so, we simply compute (for each star) the distribution

$$P(e) = \int_{i_{\text{C}CW}} P(i_{\text{C}CW}, e) P(i_{\text{C}CW}) di_{\text{C}CW}, \quad (\text{C1})$$

where  $P(i_{\text{C}CW})$  is known a priori: a Gaussian centered on 0 and of width  $14^\circ$  and  $19^\circ$ , respectively, for the CWS and CCWS. We then fit a Gaussian on this distribution and take the centroid as the best estimate and the width of the Gaussian as the uncertainty.

It must be understood that the histograms are sometimes not nearly Gaussian. The method gives reasonable estimates given the quoted error bars, however.

## APPENDIX D

### LIKELIHOOD THAT IRS 13E IS A BACKGROUND FLUCTUATION

In § 3.3.1 we use stellar counts to show that IRS 13E is not a background density fluctuation. The first step is to determine the background density. We have made the approximation that, given  $\Lambda$ , the number of stars observed in the outside field of surface  $A_{\text{out}}$ , the probability  $P_N$  that the actual background density of stars is indeed  $N$  per such area is given by a Poisson law of parameter  $\Lambda$ . In our case,  $\Lambda = 115$  to a limiting magnitude of  $m_H = 20.4$  (69 to  $m_H = 19.4$ ) and  $A_{\text{out}} = 8.79 \text{ arcsec}^2$ .

Given  $N$ , the probability  $P_{N_{\text{in}}|N}$  to find  $N_{\text{in}} = 46$  (26) stars in the circular aperture of surface  $A_{\text{in}} = 1.45 \text{ arcsec}^2$  is also given by a Poisson law, of parameter  $NA_{\text{in}}/A_{\text{out}}$ . The probability, given our observations, that IRS 13E is but a spike in the Poisson noise of the background density of stars (i.e., a chance alignment) is given by the sum

$$\int_{N=0}^{+\infty} P_N P_{N_{\text{in}}|N} dN \simeq \sum_{N=0}^{+\infty} P_N P_{N_{\text{in}}|N}. \quad (\text{D1})$$

We find that the probability to find just by chance such a concentration of stars at any randomly selected line of sight in the central parsec is  $2 \times 10^{-6}$  ( $2 \times 10^{-4}$ ). The overdensity in IRS 13E is significant at the  $4.5 \sigma$  ( $3.5 \sigma$ ) level. Of course, if one selects a large number of lines of sight, the probability that one of these lines will be associated with such a chance overdensity is higher than these numbers. The question thus arises whether the choice of the location of IRS 13E can be considered as random with respect to the problem of chance alignment of stars. As discussed in § 3.3, the properties of IRS 13E make this source unique in the central parsec. However, one of the criteria for the selection of this field was the presence of three stars. Therefore, inasmuch as we subtract these three stars from our count numbers, we can consider the aperture around IRS 13E as randomly chosen. Given the number of stars that remain after having subtracted these three, the probability that the observed overdensity associated with IRS 13E is but a chance alignment remains  $2 \times 10^{-5}$  ( $2 \times 10^{-3}$ ).

## APPENDIX E

### STELLAR POPULATION SYNTHESIS

We used the synthesis code developed by Schaerer & Vacca (1998). They distinguished several subtypes of W-R stars from O (and Of) stars. They defined any star burning H in its core and having effective temperatures larger than 33,000 K as an O star. Here we are more generally interested in a population of hot stars (O I–V + B I). We therefore modify their definition of an “O” star to include the B supergiants, but not the B dwarfs, which we have not detected. In addition to this, the effective temperature of O stars has recently been revised downward (Martins et al. 2002, 2005; Crowther et al. 2002; Markova et al. 2004; Massey et al. 2005). In order to satisfy both points, we have considered as an O star in the code every star with  $T_{\text{eff}} > 23,000 \text{ K}$  and  $\log(L/L_\odot) > 5.2$ . We used Geneva evolutionary tracks with rotation (Meynet & Maeder 2003; Maeder & Meynet 2004) for both solar and twice solar metallicity. We chose the minimum masses for W-R stars according to the predictions of Meynet & Maeder (2003). An IMF with a minimum mass of  $0.8 M_\odot$  and a maximum mass of  $100 M_\odot$  was used, and we varied the slope between  $-2.35$  (Salpeter) and  $-1.35$  (top-heavy). We computed models for an instantaneous burst of star formation, an extended burst (2 Myr), and a constant formation rate.

## APPENDIX F

### DETERMINATION OF $T_{\text{eff}}$ AND $M_K$

Accurate  $T_{\text{eff}}$  values are usually derived through detailed modeling of the spectra with atmosphere codes. This is a very long process, but first insights can be obtained with “effective temperature scales” (e.g., Martins et al. 2005). In this way we were able to

assign a spectral type to most of the stars observed so far. Absolute  $K$ -band magnitudes can be easily computed from the observed  $K$  magnitudes, the distance to the GC, and an estimate of the extinction. We used the currently best GC distance ( $7.62 \pm 0.32$  kpc; Eisenhauer et al. 2005). We applied the extinction map of Scoville et al. (2003) to estimate the  $K$ -band extinction  $A_K$ . To convert the  $V$ -band extinction  $A_V$  into  $A_K$ , we have used the approximate relation  $A_K \simeq 0.1A_V$ . The resulting absolute magnitudes (and their  $1\sigma$  uncertainties) are given in the last column of Table 2. For the 8 kpc distance adopted for the rest of this paper magnitudes would be increased by  $\simeq 0.1$  mag. We applied the effective temperature scale of Martins et al. (2005) for O stars. For B stars we relied on the relations of Schmidt-Kaler (1982). In practice, for a star classified as O9–B1 I, we have chosen the effective temperature of a B0 supergiant as representative and the most likely range of values was chosen by adopting  $T_{\text{eff}}$  values for an O9 and a B1 supergiant as limiting values.

## REFERENCES

- Alexander, T. 2005, *Phys. Rep.*, 419, 65  
 Alexander, T., & Livio, M. 2004, *ApJ*, 606, L21  
 Allen, D. A., Hyland, A. R., & Hillier, D. J. 1990, *MNRAS*, 244, 706  
 Aller, L. H., et al. 1982, *Landolt-Börnstein Numerical Data and Relationships in Science and Technology*, Vol. 2 (Berlin: Springer)  
 Baganoff, F. K., et al. 2003, *ApJ*, 591, 891  
 Becklin, E. E., & Neugebauer, G. 1975, *ApJ*, 200, L71  
 Beloborodov, A. M., & Levin, Y. 2004, *ApJ*, 613, 224  
 Beloborodov, A. M., Levin, Y., Eisenhauer, F., Genzel, R., Paumard, T., Gillessen, S., & Ott, T. 2006, *ApJ*, in press  
 Blum, R. D., Ramirez, S. V., Sellgren, K., & Olsen, K. 2003, *ApJ*, 597, 323  
 Blum, R. D., Sellgren, K., & DePoy, D. L. 1995, *ApJ*, 440, L17  
 ———. 1996, *AJ*, 112, 1988  
 Bonnet, H., et al. 2003, *Proc. SPIE*, 4839, 329  
 ———. 2004, *Messenger*, 117, 17  
 Clenet, Y., et al. 2004, *A&A*, 417, L15  
 Collin, S., & Hure, J.-M. 1999, *A&A*, 341, 385  
 Crowther, P. A., Hillier, D. J., Evans, C. J., Fullerton, A. W., DeMarco, O., & Willis, A. J. 2002, *ApJ*, 579, 774  
 Davies, M. B., & King, A. 2005, *ApJ*, 624, L25  
 Diolaiti, E., Bendinelli, O., Bonaccini, D., Close, L., Currie, D., & Parmeggiani, G. 2000, *A&AS*, 147, 335  
 Eisenhauer, F., et al. 2003a, *Messenger*, 113, 17  
 ———. 2003b, *Proc. SPIE*, 4841, 1548  
 ———. 2005, *ApJ*, 628, 246  
 Figer, D. 2003, *Astron. Nachr. Suppl.*, 324, 255  
 Figer, D. F., Kim, S. S., Morris, M., Serabyn, E., Rich, R. M., & McLean, I. S. 1999, *ApJ*, 525, 750  
 Figer, D. F., McLean, I. S., & Najarro, F. 1997, *ApJ*, 486, 420  
 Forrest, W. J., Shure, M. A., Pipher, J. L., & Woodward, C. A. 1987, in *AIP Conf. Proc.* 155, *The Galactic Center*, ed. D. Backer (New York: AIP), 153  
 Gammie, C. F. 2001, *ApJ*, 553, 174  
 Genzel, R., Eckart, A., & Ott, T. 1997, *MNRAS*, 291, 219  
 Genzel, R., Pichon, C., Eckart, A., Gerhard, O., & Ott, T. 2000, *MNRAS*, 317, 348  
 Genzel, R., Thatte, N., Krabbe, A., Kroker, H., & Tacconi-Garman, L. E. 1996, *ApJ*, 472, 153  
 Genzel, R., & Townes, C. H. 1987, *ARA&A*, 25, 377  
 Genzel, R., et al. 2003, *ApJ*, 594, 812  
 Gerhard, O. 2001, *ApJ*, 546, L39  
 Ghez, A. M., Salim, S., Hornstein, S. D., Tanner, A., Morris, M., Becklin, E. E., & Duchene, G. 2005, *ApJ*, 620, 744  
 Ghez, A. M., et al. 2003, *ApJ*, 586, L127  
 Goldreich, P., & Sari, R. 2003, *ApJ*, 585, 1024  
 Goodman, J. 2003, *MNRAS*, 339, 937  
 Goodman, J., & Tan, J. C. 2004, *ApJ*, 608, 108  
 Gould, A., & Quillen, A. C. 2003, *ApJ*, 592, 935  
 Gürkan, M. A., Freitag, M., & Rasio, F. A. 2004, *ApJ*, 604, 632  
 Gürkan, M. A., & Rasio, F. A. 2005, *ApJ*, 628, 236  
 Hall, D. N. B., Kleinmann, S. G., & Scoville, N. Z. 1982, *ApJ*, 260, L53  
 Hansen, B. M. S., & Milosavljevic, M. 2003, *ApJ*, 593, L77  
 Hanson, M. M., Conti, P. S., & Rieke, M. J. 1996, *ApJS*, 107, 281  
 Hanson, M. M., Kudritzki, R. P., Kenworthy, M. A., Puls, J., & Tokunaga, A. T. 2005, *ApJS*, 161, 154  
 Horrobin, M., et al. 2004, *Astron. Nachr.*, 325, 88  
 Jackson, J. M., Geis, N., Genzel, R., Harris, A. I., Madden, S., Poglitsch, A., Stacey, G. J., & Townes, C. H. 1993, *ApJ*, 402, 173  
 Kim, S. S., Figer, D. F., & Morris, M. 2004, *ApJ*, 607, L123  
 Kim, S. S., & Morris, M. 2003, *ApJ*, 597, 312  
 Krabbe, A., Genzel, R., Drapatz, S., & Rotaciuc, V. 1991, *ApJ*, 382, L19  
 Krabbe, A., et al. 1995, *ApJ*, 447, L95  
 Langer, N. 1992, *A&A*, 265, L17  
 Lejeune, T., & Schaerer, D. 2001, *A&A*, 366, 538  
 Lenzen, R., et al. 2003, *Proc. SPIE*, 4841, 944  
 Levin, Y. 2006, *MNRAS*, submitted (astro-ph/0603583)  
 Levin, Y., & Beloborodov, A. M. 2003, *ApJ*, 590, L33  
 Lin, D. N. C., & Pringle, J. E. 1987, *MNRAS*, 225, 607  
 Lissauer, J. J. 1987, *Icarus*, 69, 249  
 Liszt, H. S. 2003, *A&A*, 408, 1009  
 Lu, J. R., Ghez, A. M., Hornstein, S. D., Morris, M., & Becklin, E. E. 2005, *ApJ*, 625, L51  
 Maeder, A., & Meynet, G. 2004, *A&A*, 422, 225  
 Maillard, J.-P., Paumard, T., Stolovy, S. R., & Rigault, F. 2004, *A&A*, 423, 155  
 Markova, N., Puls, J., Repolust, T., & Markov, H. 2004, *A&A*, 413, 693  
 Martins, F., Schaerer, D., & Hillier, D. J. 2002, *A&A*, 382, 999  
 ———. 2005, *A&A*, 436, 1049  
 Mas-Hesse, J. M., & Kunth, D. 1991, *A&AS*, 88, 399  
 Massey, P., Puls, J., Pauldrach, A. W. A., Bresolin, F., Kudritzki, R. P., & Simon, T. 2005, *ApJ*, 627, 477  
 McKee, C. F., & Tan, J. C. 2003, *ApJ*, 585, 850  
 McMillan, S. L. W., & Portegies Zwart, S. F. 2003, *ApJ*, 596, 314  
 Meynet, G., & Maeder, A. 2003, *A&A*, 404, 975  
 Mezger, P. G., Duschl, W., & Zylka, R. 1996, *A&A Rev.*, 7, 289  
 Milosavljevic, M., & Loeb, A. 2004, *ApJ*, 604, L45  
 Morris, M. 1993, *ApJ*, 408, 496  
 Morris, M., & Serabyn, E. 1996, *ARA&A*, 34, 645  
 Morris, P. W., Eenens, R. P. J., Hanson, M. M., Conti, P. S., & Blum, R. D. 1996, *ApJ*, 470, 597  
 Muno, M. P., Pfahl, E., Baganoff, F. K., Brandt, W. N., Ghez, A., Lu, J., & Morris, M. R. 2005, *ApJ*, 622, L113  
 Najarro, F., Hillier, D. J., Kudritzki, R. P., Krabbe, A., Genzel, R., Lutz, D., Drapatz, S., & Geballe, T. R. 1994, *A&A*, 285, 573  
 Najarro, F., Krabbe, A., Genzel, R., Lutz, D., Kudritzki, R. P., & Hillier, D. J. 1997, *A&A*, 325, 700  
 Nayakshin, S. 2005, *MNRAS*, submitted (astro-ph/0512255)  
 Nayakshin, S., & Cuadra, J. J. 2005, *A&A*, 437, 437  
 Nayakshin, S., Dehnen, W., Cuadra, J., & Genzel, R. 2006, *MNRAS*, 366, 1410  
 Nayakshin, S., & Sunyaev, R. 2005, *MNRAS*, 364, L23  
 Paumard, T., Genzel, R., Maillard, J.-P., Ott, T., Morris, M. R., Eisenhauer, F., & Abuter, R. 2004a, in *Young Local Universe*, ed. A. Chalabaev et al. (Paris: Éditions Frontières), 377  
 Paumard, T., Maillard, J.-P., & Morris, M. 2004b, *A&A*, 426, 81  
 Paumard, T., Maillard, J.-P., Morris, M., & Rigault, F. 2001, *A&A*, 366, 466  
 Portegies Zwart, S. F., & McMillan, S. L. W. 2002, *ApJ*, 576, 899  
 Portegies Zwart, S. F., McMillan, S. L. W., & Gerhard, O. 2003, *ApJ*, 593, 352  
 Reid, M. J., & Brunthaler, A. 2004, *ApJ*, 616, 872  
 Revnivtsev, M. G., et al. 2004, *A&A*, 425, L49  
 Rousset, G., et al. 2003, *Proc. SPIE*, 4839, 140  
 Sanders, R. H. 1998, *MNRAS*, 294, 35  
 Schaerer, D., Contini, T., Kunth, D., & Meynet, G. 1997, *ApJ*, 481, L75  
 Schaerer, D., & Vacca, W. D. 1998, *ApJ*, 497, 618  
 Schmidt-Kaler, T. 1982, in *Landolt-Börnstein*, Vol. VI/2b, ed. K. Schaifers & H. H. Voigt (Berlin: Springer), 1  
 Schödel, R., Eckart, A., Iserlohe, C., Genzel, R., & Ott, T. 2005, *ApJ*, 625, L111  
 Schödel, R., Ott, T., Genzel, R., Eckart, A., Mouawad, N., & Alexander, T. 2003, *ApJ*, 596, 1015  
 Schödel, R., et al. 2002, *Nature*, 419, 694  
 ———. 2006, *A&A*, submitted  
 Scoville, N. Z., Stolovy, S. R., Rieke, M., Christopher, M., & Yusef-Zadeh, F. 2003, *ApJ*, 594, 294  
 Shakura, N. I., & Sunyaev, R. A. 1973, *A&A*, 24, 337  
 Sternberg, A. 1998, *ApJ*, 506, 721  
 Sternberg, A., Hoffmann, T. L., & Pauldrach, A. W. A. 2003, *ApJ*, 599, 1333  
 Stolte, A., Brandner, W., Grebel, E. K., Lenzen, R., & Lagrange, A. M. 2005, *ApJ*, 628, L113  
 Svensson, R., & Zdziarski, A. 1994, *ApJ*, 436, 599

- Tamblyn, P., & Rieke, G. H. 1993, *ApJ*, 414, 573  
Tamblyn, P., Rieke, G. H., Hanson, M. M., Close, L. M., McCarthy, D. W., & Rieke, M. J. 1996, *ApJ*, 456, 206  
Tanner, A., et al. 2006, *ApJ*, 641, 891  
Thompson, T. A., Quataert, E., & Murray, N. 2005, *ApJ*, 630, 167  
Toomre, A. 1964, *ApJ*, 139, 1217  
Trippe, S., et al. 2006, *A&A*, 448, 305  
Vacca, W. D., & Conti, P. S. 1992, *ApJ*, 401, 543  
Wallace, L., & Hinkle, K. 1997, *ApJS*, 111, 445  
Zhao, J. H., & Goss, W. M. 1998, *ApJ*, 499, L163